

Exe.py: Ab initio fine structure parameters for trigonal defect qubits within the $E \otimes e$ Jahn-Teller case

Balázs Tóth^{a,b}, Ádám Gali^{b,a,c}, Gergő Thiering^{b,*}

^aDepartment of Atomic Physics, Institute of Physics, Budapest University of Technology and Economics, Műegyetem rakpart 3., H-1111 Budapest, Hungary

^bHUN-REN Wigner Research Centre for Physics, Institute for Solid State Physics and Optics, P.O. Box 49, H-1525 Budapest, Hungary

^cMTA-WFK Lendület "Momentum" Semiconductor Research Group, P.O. Box 49, H-1525 Budapest, Hungary

Abstract

Trigonal solid-state defects are often subjects of spontaneous symmetry breaking driven by the $E \otimes e$ Jahn-Teller effect, reflecting strong electron-phonon coupling. These systems, particularly paramagnetic defect qubits in solids are central for quantum technology applications, where accurate knowledge of their fine-structure parameters – shaped by the complex interplay of spin-orbit and electron-phonon interactions – is essential. We introduce the Exe.py code part of the jahn-teller-dynamics package, a Python code that implements the first-principles approach of [Phys. Rev. X 8, 021063 (2018)] to accurately compute the spin-orbit-phonon entanglement in trigonal defects utilizing the output from density functional theory calculations (DFT). By employing Δ SCF calculations, the method extends naturally to excited states and predicts fine-structure parameters of zero-phonon lines (ZPLs), including Zeeman shifts under external magnetic fields. The approach is applicable not only to solid-state defects but also to Jahn-Teller active trigonal molecules such as the XCH_3 family. We demonstrate the capabilities of Exe.py through applications to negatively charged Group-IV–vacancy (G4V) defects in diamond: SiV^- , GeV^- , SnV^- , PbV^- and the neutral N_3V^0 defect in diamond, and the CH_3O methoxy molecule.

Keywords: Jahn-Teller effect, $E \otimes e$ problem, Spin-orbit coupling, First principles, Density functional theory

PROGRAM SUMMARY/NEW VERSION PROGRAM SUMMARY

Program Title: Exe.py

CPC Library link to program files: (to be added by Technical Editor)

Planned to use the HUN-REN ARP data Repository *Developer's*

repository link: <https://github.com/tbalu98/Jahn-Teller-Dynamics>

<https://pypi.org/project/jahn-teller-dynamics/>

Code Ocean capsule: (to be added by Technical Editor)

Licensing provisions(please choose one): GPLv3

Programming language: Python 3.10

Supplementary material:

*Journal reference of previous version:**

*Does the new version supersede the previous version?:**

*Reasons for the new version:**

*Summary of revisions:**

Nature of problem(approx. 50-250 words):

Orbital degeneracy in trigonal solid state defects often leads to anomalous physical phenomena due to dynamic Jahn-Teller distortion. Indeed, DFT calculations within the Born-Oppenheimer approximation can be employed to determine the electronic structure in different geometrical configurations or determine the spin-orbit coupling strength. However, in order to solve Jahn-Teller problem one has to go beyond the Born-Oppenheimer approximation that is usually well beyond the capabilities of current state-of-art DFT codes. Therefore, a first-principles approach is necessary to accurately determine the fine-structure parameters such as the spin-orbit splitting visible in optical measurements utilizing trigonal color centers and molecules.

Solution method(approx. 50-250 words):

The Exe.py Python code part of the jahn-teller-dynamics package that performs the methodology developed in Refs. [1, 2]. It utilizes the results directly obtained from the VASP[3] density functional theory (DFT) code to formulate the Hamiltonian of the $E \otimes e$ Jahn-Teller case. Our solution includes the non-perturbative effect of spin-orbit coupling and the dynamic Jahn-Teller interaction simultaneously, where we observe that these two interactions non-trivially entangle with each other. Our methodology determines the damping of experimentally visible spin-orbit splitting known as Ham [4, 5, 6] reduction factor p that can be identified as electron-phonon renormalization of physical observables such as the renormalization of spin-orbit coupling strength [7, 8, 9, 10] that of trigonal defects. Our code provides a framework that automatically reads and post-processes the DFT results to compute fine-structure parameters and it includes the effect of external magnetic fields.

Additional comments including restrictions and unusual features (approx. 50-250 words):

1. Introduction

Point defects, such as vacancies, dopants and defect complexes in semiconductors and insulators such as diamond and silicon carbide hold great promise to realize solid-state quantum bits [11, 12, 13, 14, 15, 16]. The optically active quantum bit candidates are fluorescent exhibiting coherent emission within their zero-phonon-line (ZPL) which play a crucial role in setting, manipulating and readout of defect-based quantum bits fully optically [17, 18, 19, 20, 21, 22, 23, 24, 25, 26].

*Corresponding author.

E-mail address: thiering.gergo@wigner.hun-ren.hu

The underlying defect quantum bits often exhibit high symmetry, giving rise to degenerate orbitals that couple to spin, resulting in fine-structure splitting, and interact strongly with phonons also known as vibronic states. According to dynamic Jahn-Teller theory, which goes beyond the standard adiabatic approximation [27, 28, 29, 30], the strong electron-phonon interaction can quench orbital angular momentum and thereby reduce the effective spin-orbit coupling [1, 2].

In this work, we introduce `Exe.py`, an open-source Python code designed to simulate the fine structure parameters governing ZPL transitions of these defects under applied magnetic fields, using input from density functional theory (DFT) calculations. We note that our scheme can be applied to dynamic Jahn-Teller active trigonal molecules mostly exhibiting the XCH_3 structure where $X = Cd, Zn, Mg, Ca, O, Sr$, etc. [31, 32, 5, 33, 34, 35, 36, 37, 38, 39, 40, 41, 42, 43]. The code is developed using widely adopted scientific libraries such as NumPy, Pandas, SciPy, and Matplotlib. It implements the formalism presented in Refs. [1, 2], allowing direct comparison with experimental observations.

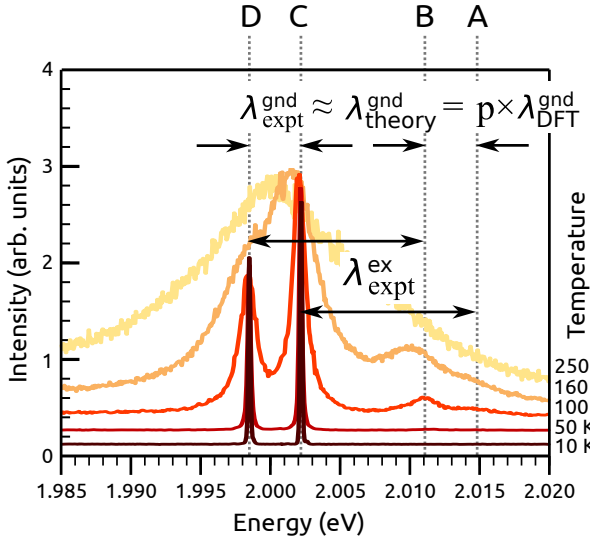


Figure 1: Relationship between the experimentally observed photoluminescence spectrum of SnV^- and the theoretical value of spin-orbit coupling $\lambda_{\text{expt, theory}}^{\text{gnd, ex}}$ of the ground (gnd) and excited (ex) states. The data for the experimental spectrum is taken from Ref. [25].

Notable examples of such defects include nitrogen-vacancy center [17, 18] and group-IV-vacancy centers [2] in diamond or silicon-vacancy [44, 45, 46, 47] and divacancy centers [48, 49, 50, 51] in silicon carbide where other host materials with defects [13] and molecular systems [52] have recently emerged as quantum bit candidates. Exemplarily, we compare the experimental ZPL spectrum that of SnV^- [25] with our theoretically predicted spin-orbit coupling fine structure parameters ($\lambda_{\text{expt/theory}}^{\text{gnd/ex}}$) in Fig. 1.

2. Basic theory

The general purpose of `jahn-teller-dynamics` is to evaluate the following [2, 29, 53] following interaction Hamiltonian

$$\hat{H} = \hat{H}_{\text{SOC}} + \hat{H}_{\text{vib}} + \hat{H}_{\text{DJT}} + \hat{H}_{\text{ext}}, \quad (1)$$

to theoretically predict the fine structure details for defects such as the $\lambda_{\text{theory}} \approx \lambda_{\text{expt}}$ spin-orbit splitting parameter visible in experiments. In

the following sections, we describe the terms of Eq. (1). First, we discuss the intrinsic spin-orbit coupling \hat{H}_{SOC} in Sec. 2.1, that we determine by means of DFT calculations. Next, we introduce the dynamic Jahn-Teller effect in Sec. 2.2 where \hat{H}_{vib} depicts the atomic vibrations that are represented by quantum harmonic oscillators while \hat{H}_{DJT} is the electron-phonon interaction term due to the dynamical Jahn-Teller effect. Finally, the code directly diagonalizes \hat{H} yielding the theoretical spin-orbit-phonon spectrum (see Sec. 2.3 for details). The last term ($\hat{H}_{\text{ext}} = \hat{H}_{\text{mag.}} + \hat{H}_{\text{strain}}$) depicts the coupling of electronic orbital and spin with external magnetic field, electric field and strain that we discuss in Section 2.4.

We note that the fine structure parameters can be encompassed into an effective model Hamiltonian for the vibronic ground state where the vibronic degrees of freedom (X, Y) can be traced out [2, 6] by averaging over the phonon bath. We discuss the properties of the effective Hamiltonian in Sec. 2.5 where the intrinsic λ_{DFT} spin-orbit parameter is renormalized into an effective $\lambda_{\text{theory}} = p \times \lambda_{\text{DFT}} \approx \lambda_{\text{expt}}$ energy gap visible in experiments through the introduction of Ham reduction factors. Whenever both ground and optical excited states are dynamic Jahn-Teller active multiplets, then Eq. (1) can be applied for both states to determine the fine structure features in the optical spectra. In such systems, `jahn-teller-dynamics` can simulate the fine levels in the optical spectrum as schematically depicted in Figs. 2 and 5.

Finally, we exemplarily depict the workflow with our code on experimentally known defects such as G4V defects (SiV, GeV, SnV, PbV) in Sec. 3 including computational details (Sec. 3.1), where we highlight the N_3V^0 defect (Sec. 3.3) whose spin-orbit parameter was not been determined by ab-initio tools and compared to experimental data to our best knowledge.

2.1. Trigonal system and spin-orbit coupling

We investigate point defects in solids exhibiting trigonal symmetry and electronically degenerate states. According to Jahn-Teller theory, such degenerate many-body electronic states undergo spontaneous symmetry breaking due to geometrical distortions. In this context, adiabatic approximation generally breaks down for degenerate (or quasi-degenerate) many-body electronic defect states in solids, owing to strong electron-phonon interaction. In this work, we focus on defects exhibiting trigonal point-group symmetries such as D_{3d} and C_{3v} that can feature double degenerate orbitals or phonons labeled as "E" or "e" in Schönflies notation. For the D_{3d} point group, parity labels are omitted, as they hold no relevance in the present context.

The doubly degenerate orbitals ($|e_x^{\text{DFT}}\rangle, |e_y^{\text{DFT}}\rangle$) of point defects in solids or molecules can be approximately well characterized by DFT methodology. When these degenerate Kohn-Sham orbitals are occupied by a single electron or equivalently left with a single hole results in a doubly degenerate many-body state. Furthermore, we note that taking into account the Kramers degeneracy of spin- $\frac{1}{2}$ systems yields a combined spin-orbital system exhibiting fourfold degeneracy. By performing non-collinear calculations with spin-orbit effects turned on [54], one can determine the spin-orbit splitting of these degenerate Kohn-Sham orbitals by setting half-half occupation of the degenerate Kohn-Sham levels [1, 2]. As a consequence, the Kohn-Sham states will acquire complex-valued character:

$$|e_{\pm}^{\text{DFT}}\rangle = \mp(|e_x^{\text{DFT}}\rangle \pm i|e_y^{\text{DFT}}\rangle), \quad (2)$$

where the phases are chosen in accordance with the Condon-Shortley convention. Their energy levels are separated by

$$\lambda_{\text{DFT}} = E(e_+^{\text{DFT}}) - E(e_-^{\text{DFT}}), \quad (3)$$

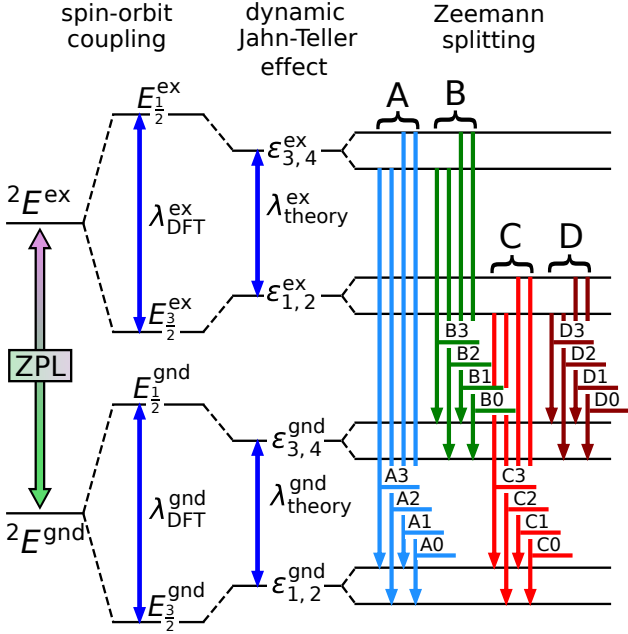


Figure 2: This figure represents the physics behind the zero-phonon-line (ZPL) transitions in trigonal point defects with degenerate electronic ground and excited states. The spin-orbit electronic states of the ground and excited state are fourfold degenerate. Due to spin-orbit coupling they split into two $E_{\frac{1}{2}}$ and $E_{\frac{3}{2}}$ multiplets and the energy difference between them is λ_{DFT} . If we take into consideration atomic vibrations by utilizing the $E \otimes e$ Jahn-Teller effect case, they will split to two distinct two-fold degenerate energy levels ($|e_1\rangle, |e_2\rangle$) and ($|e_3\rangle, |e_4\rangle$). They are entangled states of phonons, orbitals and spin. Under a constant external magnetic field the system experiences total loss of degeneracy because of Zeeman-effect. A,B,C,D represents the transition types as defined in Ref. [24].

where $E(e_{\pm}^{\text{DFT}})$ denote the eigenenergies of the corresponding orbital states. One may observe that the $\hat{L}_z = i \begin{pmatrix} 0 & -1 \\ 1 & 0 \end{pmatrix}$ assumes a simpler diagonal form upon transformation to the complex basis of Eq. (2): $\hat{L}_{z,\text{complex}} = \begin{pmatrix} 1 & 0 \\ 0 & -1 \end{pmatrix}$ which explicitly reflects $|e_{\pm}^{\text{DFT}}\rangle$'s the orbital angular momentum quantum number $m_l = \pm 1$. The spin states are $|\uparrow\rangle$ and $|\downarrow\rangle$, and the spin operator is $\hat{S}_z = \frac{1}{2} \begin{pmatrix} 1 & 0 \\ 0 & -1 \end{pmatrix}$. The spin-orbit interaction operator is

$$\hat{H}_{\text{SOC}} = \lambda_{\text{DFT}} \hat{L}_z \otimes \hat{S}_z. \quad (4)$$

As a result, we find that the fourfold degenerate electronic states split into two Kramers doublets:

$$\begin{aligned} |E_{\frac{1}{2}}\rangle &= \{|e_+^{\text{DFT}}\rangle \otimes |\downarrow\rangle, |e_-^{\text{DFT}}\rangle \otimes |\uparrow\rangle\}, \\ |E_{\frac{3}{2}}\rangle &= \{|e_-^{\text{DFT}}\rangle \otimes |\downarrow\rangle, |e_+^{\text{DFT}}\rangle \otimes |\uparrow\rangle\}. \end{aligned} \quad (5)$$

where the spin-orbit interaction shifts $|E_{\frac{1}{2}}\rangle$ upwards while $|E_{\frac{3}{2}}\rangle$ downwards in energy by $\lambda_{\text{DFT}}/2$. However, the computed λ_{DFT} substantially overestimates the experimentally measured λ_{expt} for most defect-based quantum bits [1, 2]. This discrepancy arises from strong electron-phonon coupling: where λ_{DFT} represents only the spin-orbit splitting of the unrenormalized (bare) electronic states and is subsequently reduced by the Jahn-Teller effect, as discussed in the following section.

2.2. $E \otimes e$ Jahn-Teller effect

In this section, we briefly outline how strong electron-phonon coupling in trigonal systems can partially quench the spin-orbit interaction and thereby substantially modify the effective spin-orbit splitting. Within geometry optimization workflows during DFT calculations, one may observe that low symmetry configurations (e.g. C_{2h} or

C_{1h}) are energetically favored over the high-symmetry configuration for trigonal defects. In such distorted cases $|e_x^{\text{DFT}}\rangle$ and $|e_y^{\text{DFT}}\rangle$ orbitals become non-degenerate as the phonons perturb electronic structure. These trigonal systems can be described within the framework of the $E \otimes e$ Jahn-Teller case as explained in Ref. [29]. The localized vibration (E) is also doubly degenerate, similarly to the orbital manifold, and thus it can be introduced as a two-dimensional harmonic oscillator:

$$\hat{H}_{\text{vib}} = \omega(a_x^\dagger a_x + a_y^\dagger a_y + 1), \quad (6)$$

where $a_{x,y}^\dagger$ and $a_{x,y}$ are phonon creation and annihilation operators while ω is the energy quantum of the oscillator. In an electron-phonon entangled manifold, the vibrational Hamiltonian is required to be extended to $\hat{H}_{\text{vib}} \rightarrow \hat{H}_{\text{vib}} \otimes \mathbb{1}_{\text{orb}}$ where the additional identity operator $\mathbb{1}_{\text{orb}} = \begin{pmatrix} 1 & 0 \\ 0 & 1 \end{pmatrix}$ spans the orbital degrees of freedom to the coupled system. However, from now on, we will neglect the trivial \otimes and $\mathbb{1}_{\text{orb}}$ for simplicity.

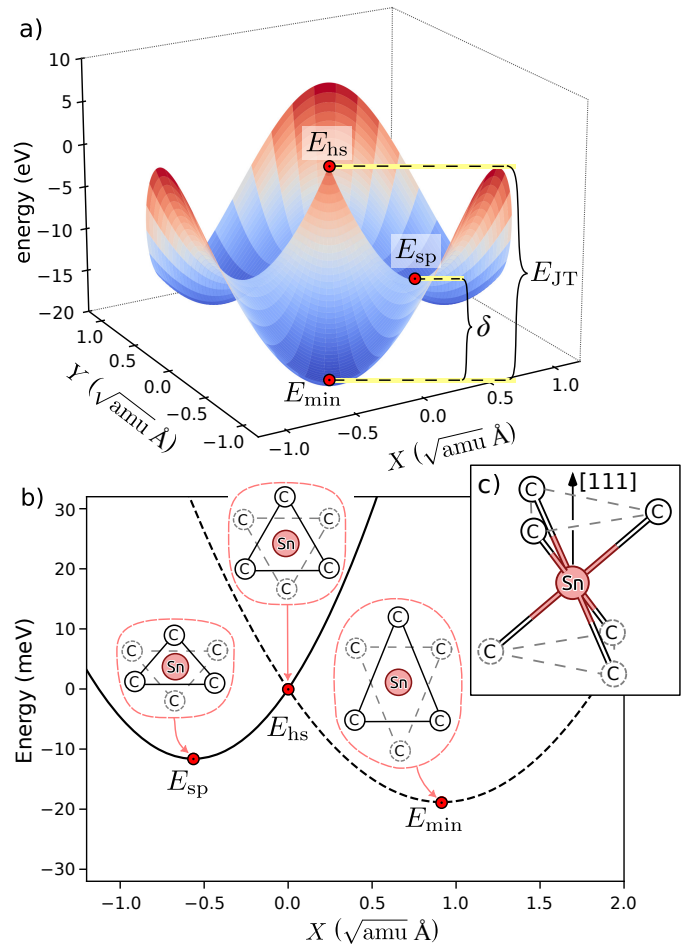


Figure 3: (a) Adiabatic potential energy surface (APES) of the Jahn-Teller distortion. An one-dimensional cut through the APES surface is shown in (b). Panel (c) displays the atomic configuration of the SnV center in diamond, with the distortions indicated in the insets that of panel (b). By applying the same distortion in two opposite directions, the global energy minimum and saddle point configurations can be found.

Within the two dimensional harmonic oscillation of the lattice couples to the doubly degenerate electron orbital states which can be described by the following Hamiltonian:

$$\hat{H}_{\text{DJT}} = F(\hat{X}\hat{\sigma}_z - \hat{Y}\hat{\sigma}_x) + G[(\hat{X}^2 - \hat{Y}^2)\hat{\sigma}_z + 2\hat{X}\hat{Y}\hat{\sigma}_x], \quad (7)$$

where \hat{X} and \hat{Y} are the position operators of the vibrational mode with energy quantum ω while $\hat{\sigma}_z = |e_x\rangle\langle e_x| - |e_y\rangle\langle e_y| = \begin{pmatrix} 1 & 0 \\ 0 & -1 \end{pmatrix}$ and $\hat{\sigma}_x = |e_x\rangle\langle e_y| + |e_y\rangle\langle e_x| = \begin{pmatrix} 0 & 1 \\ 1 & 0 \end{pmatrix}$ Pauli matrices govern the orbital degrees of freedom. The quantum states of the system thus consist of doubly degenerate orbitals entangled with two-dimensional vibrational motion. We numerically diagonalize the $\hat{H}_{\text{vib}} + \hat{H}_{\text{DJT}}$ Hamiltonian. The eigenstates of the coupled system can be expanded in the following series expansion:

$$|\kappa_i\rangle = \sum_{k,l} (c_{k,l}^{(i)} |e_x\rangle + d_{k,l}^{(i)} |e_y\rangle) \otimes |k, l\rangle, \quad (8)$$

where $|e_{x,y}\rangle$ are electronic orbitals while $|k, l\rangle$ are vibronic wavefunctions. The latter represent the Fock states of the two-dimensional quantum harmonic oscillator along X, Y directions, explicitly given by $|k, l\rangle = \frac{1}{\sqrt{k!l!}} (a_x^\dagger)^k (a_y^\dagger)^l |0, 0\rangle$. We truncate the phonons at an n -phonon limit, where $k + l \leq n$. We note that the two lowest eigenstates $|\kappa_{1,2}\rangle$ are always degenerate, thus they can be grouped as a degenerate level exhibiting E symmetry unless the quadratic coupling becomes extremely strong [29], which is not the case of normally behaved defect centers.

We now turn to the description of the DFT calculations, in which the coordinates X and Y are treated as classical configurational variables entering the total energy of the full electron-nuclear system, rather than as quantized operators. The total energy can be evaluated as a function of these distortion coordinates, thereby defining the adiabatic potential energy surface (APES). The APES, which comprises two branches as illustrated in Fig. 3, can be written as

$$E_{\pm} = \frac{1}{2} \omega R^2 \pm R \sqrt{F^2 + G^2 R^2 + 2FGR \cos(3\phi)}, \quad (9)$$

where $R = \sqrt{X^2 + Y^2}$ is the distance from the conical intersection and $\phi = \arctan(Y/X)$ is the pseudo-rotation angle. The resulting APES exhibits three types of critical points: (i) the conical intersection at due to trigonal symmetry-breaking distortions; and $X = 0, Y = 0$ where $|e_{x,y}^{\text{DFT}}\rangle$ are degenerate and exhibiting E_{hs} energy; (ii) three equivalent minima, at which the system attains its lowest total energy E_{min} due to trigonal symmetry-breaking distortion; (iii) three equivalent saddle points exhibiting E_{sd} total energy. These special configurations can be identified through geometry optimizations performed with imposed symmetry constraints. The procedure begins by initializing the atomic structure in its high-symmetry configuration – e.g., D_{3d} or C_{3v} for group-IV—vacancy centers or the NV, N_3V , (CH_3O) centers (molecule), respectively – and relaxing the atomic positions while preserving this high symmetry. Next, the lattice is distorted along $+X$, lowering the symmetry to C_{2v} or C_{1h} . Further optimizing the atomic positions by DFT yields either the saddle-point energy E_{sd} or the minimum point E_{min} ; however, at this stage it is not known which of the two has been reached. To identify the remaining configuration, one has to distort the opposite $-X$ additionally, which will identify the missing other special point. We note that retaining a mirror-symmetry constraint during the relaxation provides a practical advantage: it prevents the system from leaving the X axis and relaxing to E_{min} because the system is confined in $Y = 0$ thus ensuring both special points are being located unambiguously.

Our purpose of the DFT calculations is to parametrize the Jahn-Teller system. The full reconstruction of the APES makes possible to express the linear F and quadratic G Jahn-Teller coefficients as follows

$$F = \sqrt{2E_{\text{JT}}\omega \left(1 - \frac{\delta}{2E_{\text{JT}} - \delta}\right)} \quad \text{and} \quad G = \frac{\omega\delta}{4E_{\text{JT}} - 2\delta}, \quad (10)$$

where $E_{\text{JT}} = E_{\text{hs}} - E_{\text{min}}$ is the Jahn-Teller (JT) (stabilization) energy, $\delta = E_{\text{sp}} - E_{\text{min}}$ is the barrier height thus the quantities E_{JT} and δ

are readily obtained as total-energy differences directly from the DFT runs. To determine ω , we proceed as follows. One may fit two one-dimensional harmonic oscillators along the X coordinate (e.g. $Y = 0$) in the neighborhood of configurations E_{min} and E_{sp} . Specifically, the two oscillators will exhibit

$$\omega_{\text{min}} = \sqrt{2 \frac{E_{\text{hs}} - E_{\text{min}}}{d_{\text{min}}^2}} = \omega + 2G, \quad \omega_{\text{sp}} = \sqrt{2 \frac{E_{\text{hs}} - E_{\text{sp}}}{d_{\text{sp}}^2}} = \omega - 2G, \quad (11)$$

frequencies where d_{min} and d_{sp} denote the distances between the high-symmetry configuration and the Jahn-Teller minimum, and between the high-symmetry configuration and the saddle-point geometry, respectively. Both d_{min} and d_{sp} are generalized coordinates and can be expressed as follows:

$$d_{\text{min/sp}} = \sqrt{\sum_i (\mathbf{d}_{\text{hs},i} - \mathbf{d}_{\text{min/sp},i})^2 m_i}, \quad (12)$$

where $\mathbf{d}_{\text{hs},i}$, $\mathbf{d}_{\text{min},i}$, $\mathbf{d}_{\text{sd},i}$ depicts the Cartesian coordinates of the i -th atom in the high-symmetry, minimum, or saddle-point configuration, respectively, and m_i is the mass of the i -th nucleus. And thus finally, ω of the two-dimensional oscillator can be expressed as the average of the two frequencies: $\omega = (\omega_{\text{sp}} + \omega_{\text{min}})/2$.

We now quantify the energy splitting induced by the spin-orbit interaction, ($\hat{H}_{\text{SOC}} = \lambda_{\text{DFT}} \hat{L}_z \hat{S}_z$) acting within the subspace spanned by $|\kappa_{1,2}\rangle$. For sufficiently small λ_{DFT} , \hat{H}_{SOC} may be treated as a perturbation. By expanding $|\kappa_{1,2}\rangle$ in the real orbital basis $\{|e_x\rangle, |e_y\rangle\}$ and utilizing $\hat{L}_z = i \begin{pmatrix} 0 & -1 \\ 1 & 0 \end{pmatrix}$ one finds that the diagonal matrix elements vanish: $\langle \kappa_1 | \hat{L}_z | \kappa_1 \rangle = \langle \kappa_2 | \hat{L}_z | \kappa_2 \rangle = 0$. Only purely imaginary off-diagonal matrix elements remain, with magnitude of $|\langle \kappa_1 | \hat{L}_z | \kappa_2 \rangle| = p \times |\langle e_x | \hat{L}_z | e_y \rangle|$ where the p Ham reduction factor [4, 29] damps the L_z angular moment by vibronic coupling. Diagonalization of \hat{H}_{SOC} in the two-dimensional subspace spanned by $|\kappa_{1,2}\rangle$ shows that the bare DFT spin-orbit coupling λ_{DFT} is renormalized to an effective value:

$$\lambda_{\text{theory}}^{\text{pert}} = p \times \lambda_{\text{DFT}} \approx \lambda_{\text{expt}}. \quad (13)$$

We note that this perturbative approach is no longer valid for heavier impurities, for which λ_{DFT} is comparable or even exceeds E_{JT} . In such cases, the spin-orbit interaction can no longer be treated as a perturbation and must be included directly in the numerical diagonalization of the full Hamiltonian \hat{H} , as it can substantially affect and modify the vibronic expansion given in Eq. (8).

2.3. $E \otimes e$ Jahn-Teller interaction and spin-orbit coupling

In this section, we take into consideration an additional degrees of freedom: the electron spin of the unpaired electron (or hole) that can affect the electronic orbital through spin orbit coupling from Eq.(4). Therefore, we extend the expansion of Eq. (8) with electronic spin $|\xi\rangle = |\uparrow\rangle, |\downarrow\rangle$. Therefore, we expand the eigenstates of the full $\hat{H} = \hat{H}_{\text{SOC}} + \hat{H}_{\text{vib}} + \hat{H}_{\text{DJT}}$ Hamiltonian with the following expansion:

$$|\kappa_i\rangle = \sum_{\alpha} \sum_{\xi} \sum_{k,l} c_{k,l,\alpha,\xi}^{(i)} |e_{\alpha}\rangle \otimes |\xi\rangle \otimes |k, l\rangle, \quad (14)$$

where $m_l = \{x, y\}$ labels depict the orbital quantum number while k, l are phonon occupation numbers. We note that in this step, the Hamiltonian terms are promoted to the full vibronic-electronic-spin Hilbert space e.g.: $\hat{H}_{\text{DJT}} \rightarrow \hat{H}_{\text{DJT}} \otimes \mathbb{1}_{\text{spin}}$ (Eq. (7)), $\hat{H}_{\text{SOC}} \rightarrow \hat{H}_{\text{SOC}} \otimes \mathbb{1}_{\text{vib}}$ (Eq. (4)), $\hat{H}_{\text{vib}} \rightarrow \hat{H}_{\text{vib}} \otimes \mathbb{1}_{\text{orb}} \otimes \mathbb{1}_{\text{spin}}$ (Eq. (6)) where $\mathbb{1}_{\text{vib}}, \mathbb{1}_{\text{orb}}, \mathbb{1}_{\text{spin}}$ are identity operators for vibration, orbital, spin, respectively.

The two bare electronic spin-orbit Kramers doublets $|E_{\frac{1}{2}}\rangle, |E_{\frac{3}{2}}\rangle$ introduced in Eq. (5) are transformed into $|\tilde{E}_{\frac{1}{2}}\rangle, |\tilde{E}_{\frac{3}{2}}\rangle$ due to the combined action of dynamic Jahn-Teller effect and spin-orbit coupling. Therefore, the first four $|\varepsilon_{1-4}\rangle$ eigenstates that of Eq. (14) will correspond to the two polaronic $|\tilde{E}_{\frac{1}{2}}\rangle, |\tilde{E}_{\frac{3}{2}}\rangle$ doublets, whose energy separation is defined as

$$\lambda_{\text{theory}} = \langle \varepsilon_{3,4} | \hat{H} | \varepsilon_{3,4} \rangle - \langle \varepsilon_{1,2} | \hat{H} | \varepsilon_{1,2} \rangle \approx \lambda_{\text{expt}}, \quad (15)$$

and thus it can be identified that λ_{DFT} becomes renormalized to λ_{theory} in the combined vibronic-electronic-spin system. We note that $\lambda_{\text{theory}} = K_{\text{JT}} + \lambda_{\text{SOC}}$ can be decomposed into two parts: (i) the Jahn-Teller- and vibronic-induced term $K_{\text{JT}} = \langle \varepsilon_{3,4} | \hat{H}_{\text{DJT}} + \hat{H}_{\text{vib}} | \varepsilon_{3,4} \rangle - \langle \varepsilon_{1,2} | \hat{H}_{\text{DJT}} + \hat{H}_{\text{vib}} | \varepsilon_{1,2} \rangle$ and (ii) the spin-orbit contribution $\lambda_{\text{SOC}} = \langle \varepsilon_{3,4} | \hat{H}_{\text{SOC}} | \varepsilon_{3,4} \rangle - \langle \varepsilon_{1,2} | \hat{H}_{\text{SOC}} | \varepsilon_{1,2} \rangle$. One can clearly recognize the non-perturbative character of the spin-orbit interaction: as λ_{DFT} increases, the expansion coefficients $c_{k,l,\alpha,\xi}^{(i)}$ from Eq. (14), associated with $|\varepsilon_{1,2}\rangle$ and $|\varepsilon_{3,4}\rangle$ will gradually diverge from one another. Consequently, K_{JT} becomes increasingly pronounced, and even the term λ_{SOC} no longer same as in Eq. (13).

2.4. The case of external magnetic, electric fields and strain

External magnetic field $\vec{B} = (B_x, B_y, B_z)$ couples to both orbital (L) and spin (S) angular momentum of the electron via the Zeeman interaction:

$$\hat{H}_{\text{mag.}} = \mu_B g_L B_z \hat{L}_z + \mu_B g_S (B_x \hat{S}_x + B_y \hat{S}_y + B_z \hat{S}_z), \quad (16)$$

where $\mu_B = 0.0579$ meV/T is the Bohr magneton, and $g_S = 2.0023$ and g_L are the orbital and electron spin g -factor, respectively. We note that, here $g_L^{\text{gnd,ex}}$ factors are different values for optical ground (gnd) and excited (ex) states. Additionally, they differ from the $g_L = 1$ value observed in full rotation group $\text{SO}(3)$ because the defects we consider are exhibiting only trigonal 120° rotation symmetry thus $g_L^{\text{gnd,ex}}$ -s individual fractional values, see Appendix D in Ref. [2] or Refs. [55, 56, 57, 58] for details. Thus, the Zeeman Hamiltonian $\hat{H}_{\text{mag.}}$ will lift the Kramers degeneracy for both $|\varepsilon_{1,2}\rangle, |\varepsilon_{3,4}\rangle$ resulting in four states with distinct energies that can be seen in Fig. 2 or 5. Therefore, $\hat{H}_{\text{mag.}}$ be incorporated into the spin-orbit-phonon expansion that of Eq. (14) and then numerically determine the splitting due magnetic field. We note that the vibronic degrees of freedom can be traced out [4, 59, 6] whenever one is only interested in the lowest four $|\varepsilon_{1-4}\rangle$ and thus the orbital operators that we will discuss in the upcoming Section 2.5.

The splitting induced by local strain or external electric field can be described by [19, 60, 17, 61]

$$\hat{H}_{\text{strain}} = -\gamma_x \hat{\sigma}_z + \gamma_y \hat{\sigma}_x, \quad (17)$$

such that, in the presence of sufficiently strong strain or electric fields, the energy separation between the $|\tilde{E}_{\frac{3}{2}}\rangle$ and $|\tilde{E}_{\frac{1}{2}}\rangle$ Kramers doublets at zero magnetic field is enlarged to $\Delta > \lambda_{\text{theory}}$. Since each specific defect center experiences a distinct local strain environment and a characteristic configuration of nearby charged defects (which can generate residual electric fields), the corresponding splitting, Δ is typically an emitter-specific parameter, measured individually for each single defect. For inversion-symmetric centers such as G4V, the coupling to external electric fields vanishes. In contrast, systems lacking inversion symmetry – such as the NV center – exhibit finite electric-field coupling. However, this coupling be either an advantage or a disadvantage both. (i) NV centers are prone to spectral diffusion [62, 63, 64], in which the position of the zero-phonon line (ZPL) fluctuates over time due to charge-transfer processes involving nearby defects, thereby

complicating their use in practical qubit applications. (ii) On the other hand, the same coupling is advantageous enhancing qubit's T_2^* coherence time [2, 65, 66, 67, 68, 69, 70, 60, 71, 72] by effectively quenching the decoherence induced by thermal phonons by enlarging Δ by means of strain engineering. Here, we note that tracing over vibronic degrees of freedom is also convenient for strain: we will further discuss the Δ splitting in the following Section 2.5.

2.5. Effective model Hamiltonian

The higher-lying vibronic states $|\varepsilon_{j>4}\rangle$ appearing in Eq. (14) are irrelevant for standard optical measurements, as the system relaxes into one of the four lowest-lying states $|\varepsilon_{1-4}\rangle$ on a timescale in the \sim ps to \sim fs regime. This situation corresponds to the Kasha rule [73, 74], according to which only the vibronic ground levels are typically populated under optical excitation, unless the system is probed by ultrafast spectroscopy [75, 76, 77, 78, 79, 80], where the dynamics of these short-lived resonances can be characterized. Thus, in typical state-of-the-art experiments, an effective four-level Hamiltonian (\hat{H}_{eff}) can be employed [6, 2, 61, 81] to describe the $|\tilde{E}_{\frac{1}{2}}\rangle, |\tilde{E}_{\frac{3}{2}}\rangle$ manifold by introducing effective orbital: $\hat{L}_z^{\text{eff}} = \hat{\sigma}_y^{\text{eff}} = \begin{pmatrix} 0 & -i \\ i & 0 \end{pmatrix}$, $\hat{\sigma}_z^{\text{eff}} = \begin{pmatrix} 1 & 0 \\ 0 & -1 \end{pmatrix}$, $\hat{\sigma}_x^{\text{eff}} = \begin{pmatrix} 0 & 1 \\ 1 & 0 \end{pmatrix}$ and spin: $\hat{S}_x^{\text{eff}} = \frac{1}{2} \begin{pmatrix} 0 & 1 \\ 1 & 0 \end{pmatrix}$, $\hat{S}_y^{\text{eff}} = \frac{1}{2} \begin{pmatrix} 0 & -i \\ i & 0 \end{pmatrix}$, $\hat{S}_z^{\text{eff}} = \frac{1}{2} \begin{pmatrix} 1 & 0 \\ 0 & -1 \end{pmatrix}$ operators:

$$\begin{aligned} \hat{H} &= \underbrace{\hat{H}_{\text{SOC}}}_{\Downarrow} + \underbrace{\hat{H}_{\text{vib}} + \hat{H}_{\text{DJT}} + \hat{H}_{\text{mag.}}}_{\Downarrow\Downarrow} + \underbrace{\hat{H}_{\text{strain}}}_{\Downarrow} \\ \hat{H}_{\text{eff}} &= \lambda_{\text{theory}} \hat{L}_z^{\text{eff}} \hat{S}_z^{\text{eff}} + \mu_B (f B_z \hat{L}_z^{\text{eff}} + 2\delta_f B_z \hat{S}_z^{\text{eff}}) \\ &\quad + \mu_B g_S (B_x \hat{S}_x^{\text{eff}} + B_y \hat{S}_y^{\text{eff}} + B_z \hat{S}_z^{\text{eff}}) \\ &\quad - \gamma_x^{\text{eff}} \hat{\sigma}_z^{\text{eff}} + \gamma_y^{\text{eff}} \hat{\sigma}_x^{\text{eff}} \end{aligned} \quad (18)$$

The first term represents the effective spin-orbit coupling (λ_{theory}). The subsequent terms describe the interaction of the magnetic field with the effective orbital and spin angular momenta of the electron. We note that $f = p g_L$ indicates that the orbital g -factor associated with L_z is reduced by the Ham reduction factor p , since the orbital Zeeman term in Eq. (16) contains the operator \hat{L}_z , which transforms according to the A_2 irreducible representation of the C_{3v} point group. Therefore, projection onto the effective subspace reduces the orbital angular momentum such that: $\langle \hat{L}_z \rangle_{\text{ph}} = p \hat{L}_z^{\text{eff}}$, where $\langle \dots \rangle_{\text{ph}}$ denotes averaging over the phonon bath (see Appendices A and B of Ref. [6] for details). In contrast, the spin Zeeman interaction remains unchanged in the effective model, as it involves only spin operators $\{\hat{S}_x, \hat{S}_y, \hat{S}_z\}$ and no orbital contribution. However, an additional second-order term, $2\delta_f B_z \hat{S}_z^{\text{eff}}$ may arise for heavier G4V centers such as SnV⁻ and PbV⁻. This contribution originates from the orbital Zeeman interaction but manifests as an effective spin operator \hat{S}_z^{eff} in the effective system, see Appendix C in Refs. [2, 82]) in the reduced Hamiltonian (see Appendix C of Refs. [2, 82]). The magnitude of this additional term can be determined utilizing the eigenstates $|\varepsilon_{1-4}\rangle$ defined in Eq. (14):

$$\delta_f = g_L \times (\langle \varepsilon_{3,4} | \hat{L}_z \hat{S}_z | \varepsilon_{3,4} \rangle + \langle \varepsilon_{1,2} | \hat{L}_z \hat{S}_z | \varepsilon_{1,2} \rangle). \quad (19)$$

Additionally, we incorporate the effect of external strain or transverse electric fields through the effective parameters γ_x^{eff} and γ_y^{eff} . The bare strain Hamiltonian \hat{H}_{strain} in Eq. (17) is renormalized by the Ham factor $q = (1 + p)/2$, because orbital operators $\{-\hat{\sigma}_z, \hat{\sigma}_x\}$ transform according to the $\{E_x, E_y\}$ irreducible representation of C_{3v} ; see the discussion below Eq. (11) in Ref. [6]. Consequently, in the effective description one obtains: $\langle \hat{\sigma}_z \rangle_{\text{ph}} = q \hat{\sigma}_z^{\text{eff}}$, $\langle \hat{\sigma}_x \rangle_{\text{ph}} = q \hat{\sigma}_x^{\text{eff}}$ which implies: $\{\gamma_x^{\text{eff}} = q \gamma_x, \gamma_y^{\text{eff}} = q \gamma_y\}$. The resulting splitting between the two Kramers doublets at zero magnetic field is then enhanced by strain as we show below:

$$\Delta = \sqrt{\lambda_{\text{theory}}^2 + 4(\gamma_x^{\text{eff}})^2 + 4(\gamma_y^{\text{eff}})^2}. \quad (20)$$

We remark that the 4×4 effective Hamiltonian \hat{H}_{eff} reproduces the spectroscopic properties of the full Hamiltonian \hat{H} in Eq. (1), while avoiding the excessive computational cost associated with explicitly treating the large number of phononic degrees of freedom. Thus, for most practical purposes, the effective model provides a sufficient and efficient description.

3. Numerical results on solid state quantum bits in diamond

In this section, we present an illustrative example fine-structure calculation for G4V centers in diamond, a class of well-studied point defects shown in Fig. 4. As a specific example, we also analyze the ZPL splitting of the SnV^- center in an external magnetic field. The electronic structures of the high-symmetry (hs), minimum energy (min), and saddle-point (sp) geometries, as well as the spin-orbit coupling, can be evaluated by means of state-of-the-art DFT methodology. The g -factor g_L , however, cannot be calculated by VASP faithfully. In certain special cases – specifically, when the relevant orbital is strongly localized on the dopant’s d -orbitals such that the entire orbital moment is confined to a single atom and contained within its PAW sphere [83, 84, 85] – g_L can be extracted directly via the LORBMOM tag [7]. For the SiV center in diamond, the orbital moment is distributed over six carbon dangling bonds (see Fig. 8 in Ref. [2]), which renders this approach inapplicable. A more sophisticated treatment – such as those implemented in advanced quantum-chemistry packages [86, 87, 88] – would be required; however, these methods can model solids only through very small finite clusters, introducing severe finite-size artifacts. In that case, the ground- and excited-state values of g_L were obtained by fitting the effective Hamiltonian to experimental data, yielding $g_L^{\text{gnd}} = 0.328$ and $g_L^{\text{exc}} = 0.782$, respectively. These values are commonly assumed to be transferable to the other G4V centers [2].

It is important to emphasize that the natural basis of the defect spin system is, in general, not aligned with the crystallographic basis vectors. In the present example, we employ a simple-cubic supercell of diamond, where the supercell lattice vectors coincide with those of the Bravais cell. G4V centers exhibit a high-symmetry axis – corresponding to the C_3 rotation axis – aligned with the [111] crystallographic direction of diamond. It is therefore natural to adopt the [111] direction as the spin quantization axis, i.e., the z -axis associated with the electronic spin operator \hat{S}_z appearing in Eq. (13). The remaining basis vectors x - and y -axes may be chosen arbitrarily, provided they are orthogonal to the z -axis and form a right-handed coordinate system for convenience. `Exe.py` requires a `.cfg` configuration file as input to specify the following attributes of the system in order to calculate the $E \otimes e$ Jahn-Teller interaction:

- `vasprun.xml` outputs of VASP DFT calculations with relaxed atomic positions at $E_{\text{hs}}, E_{\text{min}}, E_{\text{sp}}$ special points, see Fig. 3
- maximum number of phonon quanta ($k, l < n$) in Eqs. (14), (8)
- spin-orbit coupling (λ_{DFT}) as described in section 2.1

For calculating the ZPL fine structure in the presence of magnetic field, it is further necessary to specify the following parameters:

- orbital reduction factor g_L
- the basis vectors for electronic spin quantization
- range and directions of the applied magnetic field in terms of the basis vectors of geometrical configurations

The code automatically normalizes the user-specified basis vectors. The external magnetic field is then transformed into the coordinate system defined by the defect’s spin basis. The implementation is explicitly

interfaced with the VASP package [3]. Nevertheless, the code is also compatible with results from other electronic-structure calculations, since the relevant energies can be provided directly via the configuration file and the geometries can be supplied in `.csv` format. In this latter case, the user must additionally specify the following attributes in the `.cfg` file:

- energies of the geometries ($E_{\text{hs}}, E_{\text{min}}, E_{\text{sp}}$)
- basis vectors of the geometry
- atomic masses for ions

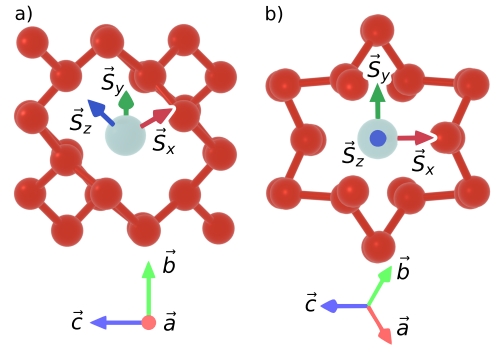


Figure 4: This figure illustrates a group-IV vacancy defect embedded in a diamond crystal. The crystallographic basis vectors ($\vec{a}, \vec{b}, \vec{c}$) are shown at the bottom of the figure in light red, green, and blue, respectively. The basis vectors for defect’s spin ($\vec{S}_x, \vec{S}_y, \vec{S}_z$) are depicted in darker shades and needs to be defined in the configuration file. For G4V centers, the spin z -axis aligns with the [111] crystallographic direction, which corresponds to the C_3 rotation axis. The two x - and y -axes can be freely chosen freely. In panel (a), the [100] crystallographic direction points toward the viewer, while in panel (b), the defect’s C_3 rotational axis points toward the viewer.

Moreover, the input may be specified either in terms of the Jahn-Teller parameters ($E_{\text{JT}}, \delta, d_{\text{min}}, d_{\text{sp}}$) or via the Taylor-expansion coefficients (F, G) of \hat{H}_{DFT} as defined in (7). All supported use cases are documented in the `configfiles` directory of the GitHub repository. The raw parameters extracted from the input files are summarized in Table 1. The code generates the following output files:

- eigenvalues and eigenstates in separate `.csv` files
- all raw parameters and theoretical values that are calculated, describes in Sec. 2
- energies of A,B,C,D transitions
- expectation values of $L_z \otimes S_z$

3.1. Computational details

The accuracy of the results obtained with `jahn-teller-dynamics` is profoundly impacted by the precision of input parameters. In this work, we employ density functional theory (DFT) within the Born-Oppenheimer approximation, as implemented in the VASP 5.4.1 code [3] within plane-wave supercell framework and projector-augmented-wave (PAW) formalism [83, 89]. We note that our code is also compatible with newer 6.x.x versions. However, we observed that numerical stability of constrained occupation Δ SCF calculations by setting `FERWE`, `FERDO` tags often vary from version to version see Refs. [90, 91] for additional details reported by other research groups. Therefore, we opted to VASP 5.4.1 where we found the best convergence over the years. Calculations are performed utilizing the Perdew-Burke-Ernzerhof (PBE) [92] generalized-gradient functional or the Heyd-Scuseria-Ernzerhof [93, 94] (HSE06) hybrid functional. Point

Table 1: Raw parameters extracted from the vasprun.xml VASP calculations supplemented with additional data for g_L and λ_{DFT} in an accompanying configuration file. Those are the energies of the high symmetric, global energy minimum and saddle point geometries ($E_{\text{hs}}, E_{\text{min}}, E_{\text{sp}}$) and the distances between them ($d_{\text{min}}, d_{\text{sp}}$). From these values the parameters of the Jahn-Teller interaction are calculated. λ_{DFT} is the energy splitting between degenerate orbitals (Kohn-Sham levels) caused by spin-orbit coupling calculated using DFT. The orbital reduction factor (g_L) appears in the magnetic field - angular momentum interaction in Eq. (16).

defect type	E_{hs} (eV)	E_{min} (eV)	E_{sp} (meV)	d_{min} ($\text{\AA}\sqrt{\text{amu}}$)	d_{sp} ($\text{\AA}\sqrt{\text{amu}}$)	g_L	λ_{DFT} (meV)
SiV gnd	-5375.9368	-5375.9791	-5375.9763	0.2085	0.2109	0.328	0.8
SiV ex	-5374.1818	-5374.2603	-5374.2577	0.3442	0.3450	0.782	6.9
GeV gnd	-5372.7556	-5372.7858	-5372.7837	0.1854	0.1884	0.328	2.2
GeV ex	-5370.5590	-5370.6440	-5370.6390	0.3574	0.3530	0.782	36.1
SnV gnd	-5368.3068	-5368.3284	-5368.3268	0.1644	0.1676	0.328	8.6
SnV ex	-5366.1366	-5366.2197	-5366.2129	0.3407	0.3421	0.782	95.9
PbV gnd	-5364.4629	-5364.4785	-5364.4779	0.1538	0.1483	0.328	34.6
PbV ex	-5361.9405	-5362.0324	-5362.0198	0.3436	0.3362	0.782	245.2

defects are modeled with an plane-wave energy cutoff of 370 eV, and strict convergence criteria on forces action on ions: 10^{-4}eV/\AA during the geometry optimization. We used 512-atom supercells to mitigate finite size effects and obtain results suitable for comparison with experiment except the spin-orbit parameters that we discuss next.

We employed the noncollinear formalism implemented in VASP 5.4.1 [85, 54] to determine the spin-orbit (λ_{DFT}) parameters. We note that fully converged spin-orbit splittings generally require supercells larger than the 512-atom cell mentioned before. The spin quantization axis was chosen along the [111] direction (C_3 rotation axis). We determine the spin-orbit parameters in supercells optimized in optimized geometries previously by means of conventional collinear calculations; thus, the influence of spin-orbit coupling on the ionic positions was neglected. The occupations of the relevant degenerate Kohn-Sham orbitals in the band gap were constrained to an equal (half-half) distribution, corresponding to a single-electron configuration ($e_{+\uparrow}^1 e_{-\uparrow}^1 e_{+\downarrow}^{0.5} e_{-\downarrow}^{0.5}$).

3.2. Optical transition energies under magnetic fields

In this section we provide exemplary calculations with the negatively charged group-IV-vacancy (G4V) defects in diamond. In these defects, the impurity atom (Si, Ge, Sn, or Pb) adopts the split-interstitial configuration (see Fig. 3(c)) exhibiting D_{3d} point group symmetry. G4V centers exhibits a ($e_u^4 e_g^3$) occupation, leaving a single hole in the degenerate e_g gerade orbital predominantly localized on carbon dangling bonds surrounding the two vacancies [82]. Their optically excited state can be characterized by ($e_g^3 e_u^4$), thus, the hole is now present in the degenerate e_u ungerade orbital. Consequently, both the ground and excited states are subjects of the $E \otimes e$ Jahn-Teller problem [2], and the corresponding spin-orbit coupling enters with negative sign, $-\lambda_{\text{DFT}}$ according to Hund's third law, that fact also visible in VASP calculations.

In order to simulate the ZPL fine structure, parameters for both ground and excited states must be specified along with the applied magnetic field. In the examples considered here, the magnetic field is aligned with the defect spin, i.e., along the [111] crystallographic direction. The script Exe.py extracts the total energies of the geometries ($E_{\text{hs}}, E_{\text{min}}, E_{\text{sp}}$), the distances between them ($d_{\text{hs}}, d_{\text{min}}, d_{\text{sp}}$), orbital g -factors, g_L , and spin-orbit λ_{DFT} parameters, are summarized in Table 1 as obtained from DFT. The code iterates over the user-specified magnetic-field range and constructs the corresponding Hamiltonian for each field value. It then computes the eigenenergies ($\{\varepsilon_i\}$ -s) for both the ground and excited states and subsequently determines the resulting ZPL fine structure, which can be directly compared with experimental observations, see Fig. 5.

At zero magnetic field, four optically allowed transitions (A, B, C, D) connect the fourfold-degenerate (e_g, e_u) manifolds (Fig. 2). Under nonzero magnetic field, each of these transitions acquires a distinct energy, giving rise to a characteristic fine structure in the spectrum with a total 16 individual transitions. In addition, the code determines the Jahn-Teller parameters and the theoretical and experimental spin-orbit splitting (λ_{theory} and λ_{expt}) that we show in Table 2.

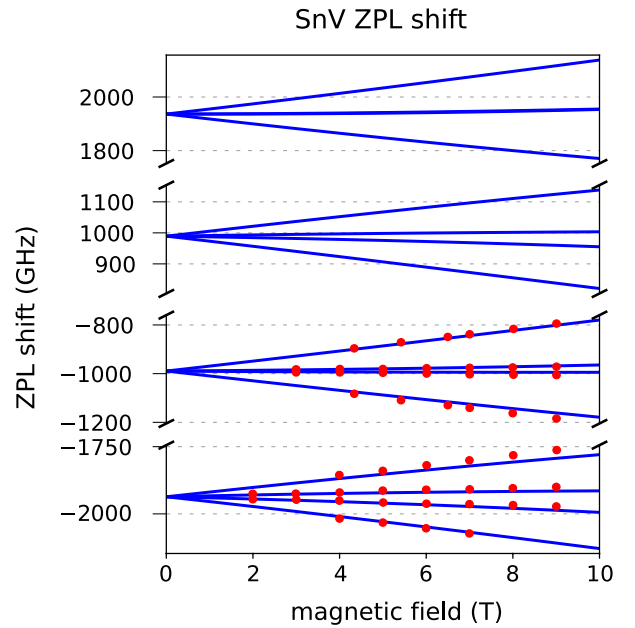


Figure 5: Magnetic field strength dependence of ZPL fine structure that of the SnV^- defect in diamond. Experimental data points are taken from Ref. [23] are compared to the result of our Exe.py code for the negatively charged SnV^- defect in diamond.

3.3. N_3V^0 defect in diamond

In this section, we demonstrate the predictive capability of our method by applying Exe.py on the neutral N_3V^0 defect in diamond. N_3V^0 center is made of three substitutional nitrogen atoms surrounding a vacancy embedded in the diamond host exhibiting C_{3v} symmetry [95]. This defect gives rise to a prominent optical feature in most type-Ia natural diamonds containing B-type nitrogen aggregates and can also be generated artificially via nitrogen ion implantation followed

Table 2: Jahn-Teller parameters and reduction factors that describe the $E \otimes e$ system, λ_{DFT} is the spin-orbit splitting calculated by DFT, E_{JT} is the Jahn-Teller energy, δ is the barrier energy, ω is the vibration energy quantum, p is the reduction factor, g_L is the orbital reduction factor, λ_{theory} is the theoretical spin-orbit splitting energy, λ_{expt} is the experimental value taken from [19],[20],[22],[26].

defect type	E_{JT} (meV)	δ (meV)	ω (meV)	p	λ_{DFT} (meV)	$\lambda_{\text{theory}}^{\text{pert.}}$ (meV)	λ_{expt} (meV)
SiV gnd	42.33	2.88	88.16	0.3163	0.8	0.25	0.3 ^[19]
SiV ex	78.51	2.68	73.7	0.1283	6.9	0.90	0.9 ^[19]
GeV gnd	30.14	2.09	83.44	0.3936	2.2	0.87	0.7 ^[20]
GeV ex	84.97	5.02	73.91	0.1168	36.1	4.21	4.6 ^[20]
SnV gnd	21.6	1.56	79.5	0.4706	8.3	3.92	3.5 ^[22]
SnV ex	83.15	6.79	75.61	0.1254	95.9	12.10	12.4 ^[22]
PbV gnd	15.62	0.6	74.94	0.4942	34.6	18.14	18.9 ^[26]
PbV ex	91.92	12.57	78.64	0.105	245.2	28.57	

Table 3: This table contains the parameters for the four state model Hamiltonian described in Eq. (18).

defect type	p	δ_p	δ_f	f	K_{JT}	$p\lambda_{\text{DFT}}$	λ_{theory}
SiV gnd	0.3163	0.0036	0.0012	0.1038	2.8971×10^{-6}	0.2530	0.2531
SiV exc	0.1284	0.0230	0.0180	0.1004	1.9766×10^{-6}	0.8859	0.8859
GeV gnd	0.3936	0.0114	0.0037	0.1291	1.1732×10^{-4}	0.8659	0.8661
GeV exc	0.1168	0.1133	0.0886	0.0914	-0.0065	4.2177	4.2112
SnV gnd	0.4706	0.0470	0.0154	0.1544	0.0104	3.9061	3.9165
SnV exc	0.1255	0.2967	0.2321	0.0981	0.0644	12.0356	12.1000
PbV gnd	0.4942	0.2105	0.0690	0.1621	1.0412	17.0988	18.1400
PbV exc	0.1051	0.6034	0.4719	0.0822	2.7996	25.7717	28.5713

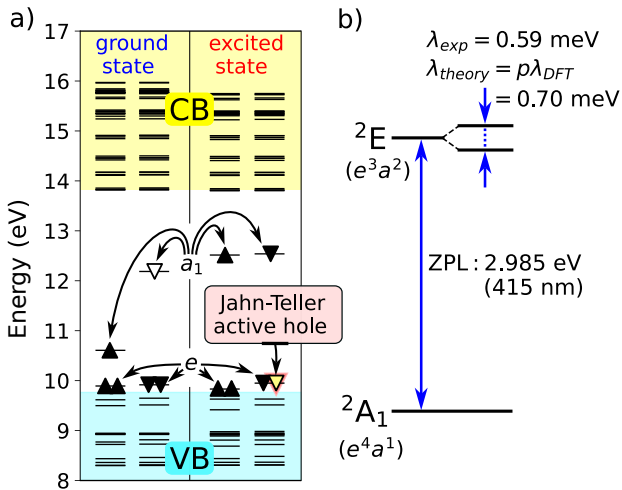


Figure 6: In the ground state configuration, e electron state is fully occupied. As we excite the system, the electron is promoted to the a_1 state and leaves a hole behind in the e state. This leads to a dynamic Jahn-Teller system in the optical excited state.

by annealing at temperatures above 1200 °C [96]. Figure 6 schematically illustrates the electronic structure of the defect: a_1 and e levels appear within the boundaries of the band gap, with the corresponding orbitals predominantly localized on carbon and nitrogen dangling bonds, respectively. In the ground state configuration (e^4a^1), the e level is fully occupied, therefore, it is not Jahn-Teller active (e^4a^1) multiplet. Upon optical excitation, an electron is promoted from the e level to the a_1 level, leaving a hole in the e level [97] and thus, the excited

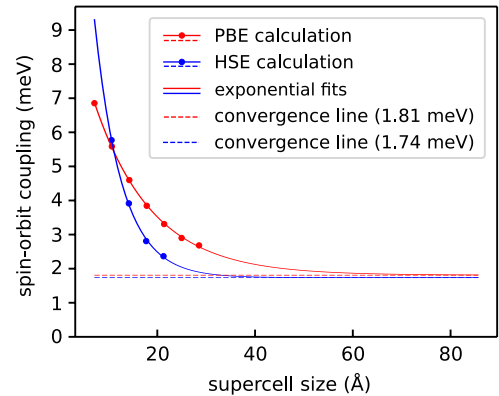


Figure 7: Spin-orbit λ_{DFT} parameters using PBE (HSE06) functional in diamond supercells with superlattices ranging 63-4095 (63-1727) atoms. Both functionals show an exponential decay with respect to supercell length converging to 1.81 meV (1.74 meV)

state is Jahn-Teller active (2E) multiplet. Experimentally, the ZPL of N_3V^0 has been reported at 2.985 eV, with a fine-structure splitting of 0.59 meV in photoluminescence (PL) spectra [96]. Utilizing the HSE06 functional, we obtain a ZPL energy as 3.059 eV, representing an improvement over an earlier (semi)local DFT result of 2.8 eV [98]. We attribute the observed ZPL splitting to spin-orbit splitting within the 2E excited state; thus, we employ our Exe.py code to calculate λ_{theory} for the PL spectrum. To generate the all input parameters for Exe.py, we performed constrained DFT calculations by means of the HSE06 functional on an 1728-atom supercell that holds 6911 valence electrons. In order to simulate the excited state (Fig. 6) we employ constrained occupation DFT calculations with FERWE = 3456 * 1.0 and FERDO = 3454 * 1.0 0.0 1.0 tags. These points perfectly fit two

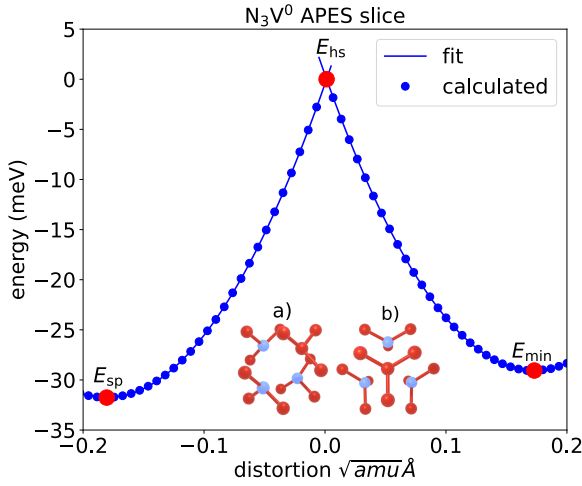


Figure 8: This figure shows the calculated APES of the excited state of the neutral N_3V^0 defect. The a) and b) part of the figure represents the N_3V^0 point defect.

quadratic polynomials that intersect exactly at the C_{3v} high-symmetry configuration, see Fig. 8. Finally, the derived Jahn-Teller energy of the system $E_{JT} = 32.12$ meV, the barrier energy $\delta = 2.68$ meV, and the vibrational energy quantum $\omega = 89.54$ meV as yielded by Exe.py code which results in a Ham reduction factor $p = 0.40$ for this system.

Next, we determine the bare spin-orbit λ_{DFT} parameter for the 2E excited state, where we force the $(e_{+\uparrow}^1 e_{-\uparrow}^1 e_{+\downarrow}^{0.5} e_{-\downarrow}^{0.5})$ occupation – for example on the 1727-atom supercell – by

$$\text{FERWE} = 3455 * 1.0 \ 3453 * 1.0 \ 0.5 \ 0.5 \ 2 * 1.0 \ 2000 * 0.0 \quad (21)$$

where Kohn-Sham energy difference between $e_{+\downarrow}$ and $e_{-\downarrow}^{0.5}$ single particle orbitals yields λ_{DFT} . We used a sequence of diamond supercells of increasing size 63, 215, 511, 999, 1727, 2743, 4095 atoms to fully avoid the spurious interaction between periodic images. Figure 7 shows the calculated spin-orbit energies λ_{DFT} as a function of supercell size; the values decrease exponentially with increasing superlattice length and converge to 1.81 meV (1.74 meV) within PBE (HSE06).

Combining this with the Ham reduction factor $p = 0.40$, we obtain an effective spin-orbit splitting $\lambda_{\text{theory}} = 0.70$ meV which is a very good agreement against the experimental data at $\lambda_{\text{expt}} = 0.59$ meV, and thus, reaffirms N_3V^0 assignment for the 3.059-eV color center in diamond.

3.4. CH_3O^0 molecule

In this section we present how our code can be used to calculate the spin-orbit coupling in the CH_3O molecule. This molecule possess C_{3v} symmetry. We performed density functional theory calculations using the PBE0 functional [99] which combines the generalized gradient functional with an amount of predefined full-range exact exchange interaction of 0.25 and uses no cutoff in the calculation of Coulomb interaction. In the ground state it has an e orbital partially filled by three electrons. The hole that represents the three electrons that occupy a fourfold degenerate spin-orbit state is dynamic Jahn-Teller active. We found the local minimum and saddle point geometrical configurations; however, in the optimization process the molecules experienced spurious translations and rotations. To eliminate these numerical artifacts, we calculated the vibrational modes by means of the PBE functional

and projected out the last six degrees modes associated with translations and rotations from atomic displacements. As a result, we found that the doubly degenerate orbital states of the CH_3O interacts with an effective vibrational mode whose frequency is 130.50 meV. We report the Ham reduction factor as $p = 0.47$. We note that, a similar quenching factor ($d = 0.478$) was reported in Ref. [100], where EOM-CCSDT/ANO1 level of theory [101] was used to characterize the potential energy surface. Moreover, we performed non-collinear calculation of the energy splitting due to spin-orbit coupling as described in Sec. 3.3. However, we had to smear the three electrons that resides on the four spin-orbital states of the e orbital by forced 0.75 occupations by $(e_{+\uparrow}^{0.75} e_{-\uparrow}^{0.75} e_{+\downarrow}^{0.75} e_{-\downarrow}^{0.75})$ occupation in order to avoid the disastrous effect of spin contamination. Otherwise, we experienced $3\times$ underestimation upon calculating λ_{DFT} within the $(e_{+\uparrow}^1 e_{-\uparrow}^1 e_{+\downarrow}^{0.5} e_{-\downarrow}^{0.5})$ constraint. Our intrinsic value of $\lambda_{DFT} = 17.99$ meV is further reduced by the Ham factor that results in $\lambda_{\text{theory}} = 8.47$ meV which is in good agreement with the experimental value $\lambda_{\text{exp}} = 7.94$ meV reported in Ref. [102].

4. Summary

In this work, we introduced Exe.py, a Python-based tool designed to model $E \otimes e$ Jahn-Teller active systems including spin-orbit coupling. The code enables accurate calculation of energy splittings induced by vibronic and spin-orbit interactions and then simulates optical transition energies in the presence of an external magnetic field – parameters of direct relevance to current experimental and theoretical studies in the recent years. Its capabilities were demonstrated by extracting key theoretical parameters for G4V centers in diamond, simulating the ZPL fine structure of the SnV^- center, and we applied the code to predict the ZPL fine structure splitting energy of the neutral N_3V^0 defect in diamond and the reduced spin-orbit coupling in the methoxy (CH_3O^0) molecule. In all cases, the results show good agreement with experimental data.

Exe.py is part of jahn-teller-dynamics package which provides a powerful and flexible platform for the $E \otimes e$ Jahn-Teller case. Beyond its present functionality, it offers a general framework for constructing quantum-mechanical models and specifying their Hamiltonians. Owing to its modular design, Exe.py can be readily extended to treat more complex scenarios, such as the $T \otimes (t+e)$ Jahn-Teller system [103, 104, 105, 106], pseudo Jahn-Teller effect [107, 108, 109, 110], and product Jahn-Teller systems [111, 112, 113, 110].

CRedit authorship contribution statement

Balázs Tóth: Writing – original draft, Software, Validation, Methodology, Investigation, Conceptualization, Data curation; **Ádám Gali:** Writing – review & editing, Supervision, Funding acquisition **Gergő Thiering:** Writing – review & editing, Supervision, Project administration, Formal analysis, Conceptualization, Validation, Funding acquisition

Data availability

The data that support the findings of this article will be openly available in the HUN-REN ARP database under the entry [xxx].

Declaration of competing interest

The authors declare that they have no known competing financial interests or personal relationships that could have appeared to influence the work reported in this paper.

Declaration of generative AI and AI-assisted technologies in the writing process

The authors used the grammar assisting tools provided by Writefull within Overleaf and ChatGPT to improve the overall readability of the text. The authors reviewed and edited the content from sentence to sentence and acted appropriately for every single suggestion made by these tools, and thus the authors take full responsibility for the content of the manuscript.

Acknowledgements

The project supported by the Doctoral Excellence Fellowship Programme (DCEP) is funded by the National Research Development and Innovation Fund of the Ministry of Culture and Innovation and the Budapest University of Technology and Economics. Support by the Ministry of Culture and Innovation and the National Research, Development and Innovation Office (NKFIH) within the Quantum Information National Laboratory of Hungary (Grant No. 2022-2.1.1-NL-2022-00004) is much appreciated. A. G. acknowledges the high-performance computational resources provided by KIFÜ (Governmental Agency for IT Development), the European Commission for the projects SPINUS (Grant No. 101135699) and QuSPARC (Grant No. 101186889) as well as the QuantERA II projects Maestro (NKFIH Grant No. 2019-2.1.7-ERA-NET-2022-00045) and Sensextreme (NKFIH Grant No. 2019-2.1.7-ERA-NET-2022-00040). G. T. was supported by the János Bolyai Research Scholarship of the Hungarian Academy of Sciences and by NKFIH under Grant No. STARTING 150113.

References

- [1] G. Thiering, A. Gali, Ab initio calculation of spin-orbit coupling for an nv center in diamond exhibiting dynamic jahn-teller effect, *Phys. Rev. B* 96 (2017) 081115. doi:10.1103/PhysRevB.96.081115. URL <https://link.aps.org/doi/10.1103/PhysRevB.96.081115>
- [2] G. Thiering, A. Gali, Ab initio magneto-optical spectrum of group-iv vacancy color centers in diamond, *Phys. Rev. X* 8 (2018) 021063. doi:10.1103/PhysRevX.8.021063. URL <https://link.aps.org/doi/10.1103/PhysRevX.8.021063>
- [3] G. Kresse, J. Furthmüller, Efficient iterative schemes for ab initio total-energy calculations using a plane-wave basis set, *Phys. Rev. B* 54 (1996) 11169–11186. doi:10.1103/PhysRevB.54.11169. URL <https://link.aps.org/doi/10.1103/PhysRevB.54.11169>
- [4] F. S. Ham, Dynamical jahn-teller effect in paramagnetic resonance spectra: Orbital reduction factors and partial quenching of spin-orbit interaction, *Phys. Rev.* 138 (1965) A1727–A1740. doi:10.1103/PhysRev.138.A1727. URL <https://link.aps.org/doi/10.1103/PhysRev.138.A1727>
- [5] G. D. Bent, Method of measuring the ham reduction factor q in $c3v$ molecules, *The Journal of Chemical Physics* 92 (3) (1990) 1547–1552. doi:10.1063/1.458085. URL <http://dx.doi.org/10.1063/1.458085>
- [6] A. Norambuena, A. Jimenez, C. Becher, J. R. Maze, Effect of phonons on the electron spin resonance absorption spectrum, *New Journal of Physics* 22 (7) (2020) 073068. doi:10.1088/1367-2630/ab9da0. URL <https://doi.org/10.1088/1367-2630/ab9da0>
- [7] A. Csóré, A. Gali, Ab initio determination of pseudospin for paramagnetic defects in sic, *Phys. Rev. B* 102 (2020) 241201. doi:10.1103/PhysRevB.102.241201. URL <https://link.aps.org/doi/10.1103/PhysRevB.102.241201>
- [8] G. Thiering, A. Gali, Photoexcitation and recombination processes of the neutral nitrogen-vacancy center in diamond from first principles, *Journal of Applied Physics* 136 (8) (Aug. 2024). doi:10.1063/5.0221228. URL <http://dx.doi.org/10.1063/5.0221228>
- [9] K. Li, V. D. Dergachev, I. D. Dergachev, S. Zhang, S. A. Varganov, Y. Ping, Excited-state dynamics and optically detected magnetic resonance of solid-state spin defects from first principles, *Phys. Rev. B* 110 (2024) 184302. doi:10.1103/PhysRevB.110.184302. URL <https://link.aps.org/doi/10.1103/PhysRevB.110.184302>
- [10] G. Thiering, A. Gali, Nuclear spin relaxation in solid state defect quantum bits via electron-phonon coupling in their optical excited state, *arXiv preprint arXiv:2402.19418* (2024). doi:10.48550/arXiv.2402.19418.
- [11] J. R. Weber, W. F. Koehl, J. B. Varley, A. Janotti, B. B. Buckley, C. G. Van de Walle, D. D. Awschalom, Quantum computing with defects, *Proceedings of the National Academy of Sciences* 107 (19) (2010) 8513–8518. doi:10.1073/pnas.1003052107. URL <http://dx.doi.org/10.1073/pnas.1003052107>
- [12] M. Atatüre, D. Englund, N. Vamivakas, S.-Y. Lee, J. Wrachtrup, Material platforms for spin-based photonic quantum technologies, *Nature Reviews Materials* 3 (5) (2018) 38–51. doi:10.1038/s41578-018-0008-9. URL <http://dx.doi.org/10.1038/s41578-018-0008-9>
- [13] G. Zhang, Y. Cheng, J.-P. Chou, A. Gali, Material platforms for defect qubits and single-photon emitters, *Applied Physics Reviews* 7 (3) (2020) 031308. doi:10.1063/5.0006075. URL <https://doi.org/10.1063/5.0006075>
- [14] L. C. Bassett, A. Alkauskas, A. L. Exarhos, K.-M. C. Fu, Quantum defects by design, *Nanophotonics* 8 (11) (2019) 1867–1888. doi:10.1515/nanoph-2019-0211. URL <http://dx.doi.org/10.1515/nanoph-2019-0211>
- [15] A. Chatterjee, P. Stevenson, S. De Franceschi, A. Morello, N. P. de Leon, F. Kuemmeth, Semiconductor qubits in practice, *Nature Reviews Physics* 3 (3) (2021) 157–177. doi:10.1038/s42254-021-00283-9. URL <http://dx.doi.org/10.1038/s42254-021-00283-9>
- [16] G. Wolfowicz, F. J. Heremans, C. P. Anderson, S. Kanai, H. Seo, A. Gali, G. Galli, D. D. Awschalom, Quantum guidelines for solid-state spin defects, *Nature Reviews Materials* 6 (10) (2021) 906–925. doi:10.1038/s41578-021-00306-y. URL <http://dx.doi.org/10.1038/s41578-021-00306-y>

- [17] M. W. Doherty, N. B. Manson, P. Delaney, F. Jelezko, J. Wrachtrup, L. C. Hollenberg, The nitrogen-vacancy colour centre in diamond, *Physics Reports* 528 (1) (2013) 1–45, the nitrogen-vacancy colour centre in diamond. doi:<https://doi.org/10.1016/j.physrep.2013.02.001>. URL <https://www.sciencedirect.com/science/article/pii/S0370157313000562>
- [18] Ádám Gali, Ab initio theory of the nitrogen-vacancy center in diamond, *Nanophotonics* 8 (11) (2019) 1907–1943 [cited 2025-07-28]. doi:10.1515/nanoph-2019-0154. URL <https://doi.org/10.1515/nanoph-2019-0154>
- [19] C. Hepp, T. Müller, V. Waselowski, J. N. Becker, B. Pingault, H. Sternschulte, D. Steinmüller-Nethl, A. Gali, J. R. Maze, M. Atatüre, C. Becher, Electronic structure of the silicon vacancy color center in diamond, *Phys. Rev. Lett.* 112 (2014) 036405. doi:10.1103/PhysRevLett.112.036405. URL <https://link.aps.org/doi/10.1103/PhysRevLett.112.036405>
- [20] E. Ekimov, S. Lyapin, K. Boldyrev, M. Kondrin, R. Khmel'nitskii, V. Gavva, T. Kotereva, M. Popova, Germanium–vacancy color center in isotopically enriched diamonds synthesized at high pressures I, *JETP Letters* 102 (2015) 701–706. doi:10.1134/S0021364015230034.
- [21] P. Siyushev, M. H. Metsch, A. Ijaz, J. M. Binder, M. K. Bhaskar, D. D. Sukachev, A. Sipahigil, R. E. Evans, C. T. Nguyen, M. D. Lukin, P. R. Hemmer, Y. N. Palyanov, I. N. Kupriyanov, Y. M. Borzdov, L. J. Rogers, F. Jelezko, Optical and microwave control of germanium-vacancy center spins in diamond, *Phys. Rev. B* 96 (2017) 081201. doi:10.1103/PhysRevB.96.081201. URL <https://link.aps.org/doi/10.1103/PhysRevB.96.081201>
- [22] T. Iwasaki, Y. Miyamoto, T. Taniguchi, P. Siyushev, M. H. Metsch, F. Jelezko, M. Hatano, Tin-vacancy quantum emitters in diamond, *Phys. Rev. Lett.* 119 (2017) 253601. doi:10.1103/PhysRevLett.119.253601. URL <https://link.aps.org/doi/10.1103/PhysRevLett.119.253601>
- [23] T. Iwasaki, Y. Miyamoto, T. Taniguchi, P. Siyushev, M. H. Metsch, F. Jelezko, M. Hatano, Tin-vacancy quantum emitters in diamond, *Phys. Rev. Lett.* 119 (2017) 253601. doi:10.1103/PhysRevLett.119.253601. URL <https://link.aps.org/doi/10.1103/PhysRevLett.119.253601>
- [24] A. E. Rugar, C. Dory, S. Sun, J. Vučković, Characterization of optical and spin properties of single tin-vacancy centers in diamond nanopillars, *Phys. Rev. B* 99 (2019) 205417. doi:10.1103/PhysRevB.99.205417. URL <https://link.aps.org/doi/10.1103/PhysRevB.99.205417>
- [25] J. Görlitz, D. Herrmann, G. Thiering, P. Fuchs, M. Gandil, T. Iwasaki, T. Taniguchi, M. Kieschnick, J. Meijer, M. Hatano, A. Gali, C. Becher, Spectroscopic investigations of negatively charged tin-vacancy centres in diamond, *New Journal of Physics* 22 (1) (2020) 013048. doi:10.1088/1367-2630/ab6631. URL <https://dx.doi.org/10.1088/1367-2630/ab6631>
- [26] S. Ditalia Tchernij, T. Lühmann, T. Herzig, J. Küpper, A. Damin, S. Santonocito, M. Signorile, P. Traina, E. Moreva, F. Celegato, S. Pezzagna, I. P. Degiovanni, P. Olivero, M. Jakšić, J. Meijer, P. M. Genovese, J. Forneris, Single-photon emitters in lead-implanted single-crystal diamond, *ACS Photonics* 5 (12) (2018) 4864–4871. arXiv:<https://doi.org/10.1021/acsp Photonics.8b01013>, doi:10.1021/acsp Photonics.8b01013. URL <https://doi.org/10.1021/acsp Photonics.8b01013>
- [27] *Proceedings of the Royal Society of London. Series A - Mathematical and Physical Sciences* 161 (905) (1937) 220–235. doi:10.1098/rspa.1937.0142, [link]. URL <http://dx.doi.org/10.1098/rspa.1937.0142>
- [28] H. C. Longuet-Higgins, in: H.w. thompson (ed.), *advances in spectroscopy II*. (1961) 429–472.
- [29] I. Bersuker, *The Jahn-Teller Effect*, Cambridge University Press, 2006.
- [30] I. Bersuker, V. Polinger, *Vibronic interactions in molecules and crystals*, Vol. 49, Springer Berlin, 2011.
- [31] T. Momose, Y. Endo, E. Hirota, T. Shida, The submillimeter-wave spectrum of the 13ch3o radical, *The Journal of Chemical Physics* 88 (9) (1988) 5338–5343. doi:10.1063/1.454593. URL <http://dx.doi.org/10.1063/1.454593>
- [32] T. Momose, Y. Endo, E. Hirota, T. Shida, Erratum: The submillimeter-wave spectrum of the 13ch3o radical [j. chem. phys. 88, 5338 (1988)], *The Journal of Chemical Physics* 90 (8) (1989) 4636–4637. doi:10.1063/1.456703. URL <http://dx.doi.org/10.1063/1.456703>
- [33] C. R. Brazier, P. F. Bernath, The $\tilde{A}^2E-\tilde{X}^2A_1$ transition of monomethyl calcium: A rotational analysis, *The Journal of Chemical Physics* 91 (8) (1989) 4548–4554. doi:10.1063/1.456742. URL <http://dx.doi.org/10.1063/1.456742>
- [34] T. A. Barckholtz, T. A. Miller, The calculation of spectroscopic jahn-teller parameters by ab initio methods, *The Journal of Physical Chemistry A* 103 (14) (1999) 2321–2336. doi:10.1021/jp983829x. URL <http://dx.doi.org/10.1021/jp983829x>
- [35] D. G. Melnik, J. Liu, M.-W. Chen, T. A. Miller, R. F. Curl, The spectroscopic characterization of the methoxy radical. III. rotationally resolved $\tilde{A}^2A_1-\tilde{X}^2E$ electronic and \tilde{X}^2E submillimeter wave spectra of partially deuterated ch2do and chd2o radicals, *The Journal of Chemical Physics* 135 (9) (Sep. 2011). doi:10.1063/1.3615724. URL <http://dx.doi.org/10.1063/1.3615724>
- [36] J. Liu, M.-W. Chen, D. Melnik, J. T. Yi, T. A. Miller, The spectroscopic characterization of the methoxy radical. i. rotationally resolved $\tilde{A}^2E-\tilde{X}^2A_1$ electronic spectra of CH₃O, *The Journal of Chemical Physics* 130 (7) (Feb. 2009). doi:10.1063/1.3072104. URL <http://dx.doi.org/10.1063/1.3072104>
- [37] M.-A. Martin-Drumel, J.-T. Spaniol, O. Chitarra, O. Pirali, H. S. P. Müller, Submillimeter-wave spectroscopy of the ch3o radical, *The Journal of Physical Chemistry A* 129 (3) (2025)

- 754–761. doi:10.1021/acs.jpca.4c07638.
URL <http://dx.doi.org/10.1021/acs.jpca.4c07638>
- [38] K. Sharma, O. A. Vasilyev, J. F. Stanton, T. A. Miller, Ab initio simulation of spin-vibronic spectra of methoxy radical, *The Journal of Chemical Physics* 162 (18) (May 2025). doi:10.1063/5.0266367.
URL <http://dx.doi.org/10.1063/5.0266367>
- [39] J. Nagesh, E. L. Sibert, J. F. Stanton, Simulation of laser excitation spectrum of ch_3o and cd_3o , *Spectrochimica Acta Part A: Molecular and Biomolecular Spectroscopy* 119 (2014) 90–99. doi:10.1016/j.saa.2013.02.037.
URL <http://dx.doi.org/10.1016/j.saa.2013.02.037>
- [40] B. A. Johnson, E. L. Sibert, Assigning the low lying vibronic states of ch_3o and cd_3o , *The Journal of Chemical Physics* 146 (17) (May 2017). doi:10.1063/1.4981795.
URL <http://dx.doi.org/10.1063/1.4981795>
- [41] K. Sharma, S. Garner, T. A. Miller, J. F. Stanton, First-principles calculation of jahn–teller rotational distortion parameters, *The Journal of Physical Chemistry A* 123 (23) (2019) 4990–5004. doi:10.1021/acs.jpca.9b03360.
URL <http://dx.doi.org/10.1021/acs.jpca.9b03360>
- [42] L. B. Knight, B. W. Gregory, D. W. Hill, C. A. Arrington, T. Momose, T. Shida, Electron-spin-resonance studies of $12\text{ch}_3\text{f}^+$, $13\text{ch}_3\text{f}^+$, and $12\text{ch}_2\text{df}^+$ in neon matrices at 4 k: Comparison with theoretical calculations, *The Journal of Chemical Physics* 94 (1) (1991) 67–79. doi:10.1063/1.460335.
URL <http://dx.doi.org/10.1063/1.460335>
- [43] M. J. Dick, P. M. Sheridan, J.-G. Wang, P. F. Bernath, High-resolution laser excitation spectroscopy of the $\tilde{A}^2E - \tilde{X}^2A_1$ transition of SrCH_3 , *The Journal of Chemical Physics* 124 (17) (May 2006). doi:10.1063/1.2189236.
URL <http://dx.doi.org/10.1063/1.2189236>
- [44] E. Janzén, A. Gali, P. Carlsson, A. Gällström, B. Magnusson, N. Son, The silicon vacancy in sic, *Physica B: Condensed Matter* 404 (22) (2009) 4354–4358. doi:https://doi.org/10.1016/j.physb.2009.09.023.
URL <https://www.sciencedirect.com/science/article/pii/S0921452609010862>
- [45] P. G. Baranov, A. P. Bundakova, A. A. Soltamova, S. B. Orlynskii, I. V. Borovykh, R. Zondervan, R. Verberk, J. Schmidt, Silicon vacancy in sic as a promising quantum system for single-defect and single-photon spectroscopy, *Phys. Rev. B* 83 (2011) 125203. doi:10.1103/PhysRevB.83.125203.
URL <https://link.aps.org/doi/10.1103/PhysRevB.83.125203>
- [46] F. Fuchs, V. A. Soltamov, S. Vāth, P. G. Baranov, E. N. Mokhov, G. V. Astakhov, V. Dyakonov, Silicon carbide light-emitting diode as a prospective room temperature source for single photons, *Scientific Reports* 3 (1) (2013) 1637. doi:10.1038/srep01637.
URL <https://doi.org/10.1038/srep01637>
- [47] M. Widmann, S.-Y. Lee, T. Rendler, N. T. Son, H. Fedder, S. Paik, L.-P. Yang, N. Zhao, S. Yang, I. Booker, A. Denisenko, M. Jamali, S. A. Momenzadeh, I. Gerhardt, T. Ohshima, A. Gali, E. Janzén, J. Wrachtrup, Coherent control of single spins in silicon carbide at room temperature, *Nature Materials* 14 (2) (2015) 164–168. doi:10.1038/nmat4145.
URL <https://doi.org/10.1038/nmat4145>
- [48] N. T. Son, P. Carlsson, J. ul Hassan, E. Janzén, T. Umeda, J. Isoya, A. Gali, M. Bockstedte, N. Morishita, T. Ohshima, H. Itoh, Divacancy in 4h-sic, *Phys. Rev. Lett.* 96 (2006) 055501. doi:10.1103/PhysRevLett.96.055501.
URL <https://link.aps.org/doi/10.1103/PhysRevLett.96.055501>
- [49] A. Gali, Time-dependent density functional study on the excitation spectrum of point defects in semiconductors, *physica status solidi (b)* 248 (6) (2011) 1337–1346. arXiv:https://onlinelibrary.wiley.com/doi/pdf/10.1002/pssb.201046254, doi:https://doi.org/10.1002/pssb.201046254.
URL <https://onlinelibrary.wiley.com/doi/abs/10.1002/pssb.201046254>
- [50] W. F. Koehl, B. B. Buckley, F. J. Heremans, G. Calusine, D. D. Awschalom, Room temperature coherent control of defect spin qubits in silicon carbide, *Nature* 479 (7371) (2011) 84–87. doi:10.1038/nature10562.
URL <https://doi.org/10.1038/nature10562>
- [51] D. J. Christle, P. V. Klimov, C. F. de las Casas, K. Szász, V. Ivády, V. Jokubavicius, J. Ul Hassan, M. Syväjärvi, W. F. Koehl, T. Ohshima, N. T. Son, E. Janzén, A. Gali, D. D. Awschalom, Isolated spin qubits in sic with a high-fidelity infrared spin-to-photon interface, *Phys. Rev. X* 7 (2017) 021046. doi:10.1103/PhysRevX.7.021046.
URL <https://link.aps.org/doi/10.1103/PhysRevX.7.021046>
- [52] S. L. Bayliss, D. W. Laorenza, P. J. Mintun, B. D. Kovos, D. E. Freedman, D. D. Awschalom, Optically addressable molecular spins for quantum information processing, *Science* 370 (6522) (2020) 1309–1312. arXiv:https://www.science.org/doi/pdf/10.1126/science.abb9352, doi:10.1126/science.abb9352.
URL <https://www.science.org/doi/abs/10.1126/science.abb9352>
- [53] K. Wang, T. Zeng, Hamiltonian formalism of spin–orbit jahn–teller and pseudo-jahn–teller problems in trigonal and tetragonal symmetries, *Physical Chemistry Chemical Physics* 21 (35) (2019) 18939–18957. doi:10.1039/c9cp03584b.
URL <http://dx.doi.org/10.1039/c9cp03584b>
- [54] S. Steiner, S. Khmelevskiy, M. Marsmann, G. Kresse, Calculation of the magnetic anisotropy with projected-augmented-wave methodology and the case study of disordered $\text{fe}_{1-x}\text{co}_x$ alloys, *Phys. Rev. B* 93 (2016) 224425. doi:10.1103/PhysRevB.93.224425.
URL <https://link.aps.org/doi/10.1103/PhysRevB.93.224425>
- [55] K. W. H. Stevens, On the Magnetic Properties of Covalent XY_6 Complexes, *Proceedings of the Royal Society of London Series A* 219 (1139) (1953) 542–555. doi:10.1098/rspa.1953.0166.
- [56] M. Gerloch, J. R. Miller, Covalence and the Orbital Reduction Factor, k , in *Magnetochemistry*, John Wiley & Sons, Ltd, 1968, pp. 1–47.

- arXiv:<https://onlinelibrary.wiley.com/doi/pdf/10.1002/9780470166116.ch1>
doi:<https://doi.org/10.1002/9780470166116.ch1>
URL <https://onlinelibrary.wiley.com/doi/abs/10.1002/9780470166116.ch1>
- [57] Z. Gajek, J. Mulak, Steven's orbital reduction factor in ionic clusters, *Journal of Magnetism and Magnetic Materials* 53 (1–2) (1985) 63–70. doi:10.1016/0304-8853(85)90130-1. URL [http://dx.doi.org/10.1016/0304-8853\(85\)90130-1](http://dx.doi.org/10.1016/0304-8853(85)90130-1)
- [58] Q. Wei, M. G. Brik, L.-X. Guo, B. Wei, Investigations of g factors for the 2e state of v2+ ions in al2o3 crystals, *Spectrochimica Acta Part A: Molecular and Biomolecular Spectroscopy* 97 (2012) 50–53. doi:10.1016/j.saa.2012.05.074. URL <http://dx.doi.org/10.1016/j.saa.2012.05.074>
- [59] F. S. Ham, Effect of linear jahn-teller coupling on paramagnetic resonance in a 2e state, *Phys. Rev.* 166 (1968) 307–321. doi:10.1103/PhysRev.166.307. URL <https://link.aps.org/doi/10.1103/PhysRev.166.307>
- [60] S. Meesala, Y.-I. Sohn, B. Pingault, L. Shao, H. A. Atikian, J. Holzgrafe, M. Gündoğan, C. Stavrakas, A. Sipahigil, C. Chia, R. Evans, M. J. Burek, M. Zhang, L. Wu, J. L. Pacheco, J. Abraham, E. Bielejec, M. D. Lukin, M. Atatüre, M. Lončar, Strain engineering of the silicon-vacancy center in diamond, *Physical Review B* 97 (20) (May 2018). doi:10.1103/physrevb.97.205444. URL <http://dx.doi.org/10.1103/PhysRevB.97.205444>
- [61] E. I. Rosenthal, C. P. Anderson, H. C. Kleidermacher, A. J. Stein, H. Lee, J. Grzesik, G. Scuri, A. E. Rugar, D. Riedel, S. Aghaieimodi, G. H. Ahn, K. Van Gasse, J. Vučković, Microwave spin control of a tin-vacancy qubit in diamond, *Phys. Rev. X* 13 (2023) 031022. doi:10.1103/PhysRevX.13.031022. URL <https://link.aps.org/doi/10.1103/PhysRevX.13.031022>
- [62] B. McCullian, H. Cheung, H. Chen, G. Fuchs, Quantifying the spectral diffusion of n-v centers by symmetry, *Phys. Rev. Appl.* 18 (2022) 064011. doi:10.1103/PhysRevApplied.18.064011. URL <https://link.aps.org/doi/10.1103/PhysRevApplied.18.064011>
- [63] J. Wolters, N. Sadzak, A. W. Schell, T. Schröder, O. Benson, Measurement of the ultrafast spectral diffusion of the optical transition of nitrogen vacancy centers in nano-size diamond using correlation interferometry, *Phys. Rev. Lett.* 110 (2013) 027401. doi:10.1103/PhysRevLett.110.027401. URL <https://link.aps.org/doi/10.1103/PhysRevLett.110.027401>
- [64] H. F. Fotso, A. E. Feiguin, D. D. Awschalom, V. V. Dobrovitski, Suppressing spectral diffusion of emitted photons with optical pulses, *Phys. Rev. Lett.* 116 (2016) 033603. doi:10.1103/PhysRevLett.116.033603. URL <https://link.aps.org/doi/10.1103/PhysRevLett.116.033603>
- [65] K. D. Jahnke, A. Sipahigil, J. M. Binder, M. W. Doherty, M. Metsch, L. J. Rogers, N. B. Manson, M. D. Lukin, F. Jelezko, Electron-phonon processes of the silicon-vacancy centre in diamond, *New Journal of Physics* 17 (4) (2015) 043011. doi:10.1088/1367-2630/17/4/043011. URL <http://dx.doi.org/10.1088/1367-2630/17/4/043011>
- [66] I. B. W. Harris, D. Englund, Coherence of group-iv color centers, *Phys. Rev. B* 109 (2024) 085414. doi:10.1103/PhysRevB.109.085414. URL <https://link.aps.org/doi/10.1103/PhysRevB.109.085414>
- [67] M. Mohseni, L. Razinkovas, V. Žalandauskas, G. m. H. Thiering, A. Gali, Magneto-optical properties of group-iv vacancy centers in diamond upon hydrostatic pressure, *Phys. Rev. B* 112 (2025) 155201. doi:10.1103/fq19-lfmv. URL <https://link.aps.org/doi/10.1103/fq19-lfmv>
- [68] J. M. Brevoord, L. G. C. Wienhoven, N. Codreanu, T. Ishiguro, E. van Leeuwen, M. Iuliano, L. De Santis, C. Waas, H. K. C. Beukers, T. Turan, C. Errando-Herranz, K. Kawaguchi, R. Hanson, Large-range tuning and stabilization of the optical transition of diamond tin-vacancy centers by in situ strain control, *Applied Physics Letters* 126 (17) (Apr. 2025). doi:10.1063/5.0251211. URL <http://dx.doi.org/10.1063/5.0251211>
- [69] X. Guo, A. M. Stramma, Z. Li, W. G. Roth, B. Huang, Y. Jin, R. A. Parker, J. Arjona Martínez, N. Shofer, C. P. Michaels, C. P. Purser, M. H. Appel, E. M. Alexeev, T. Liu, A. C. Ferrari, D. D. Awschalom, N. Deegan, B. Pingault, G. Galli, F. J. Heremans, M. Atatüre, A. A. High, Microwave-based quantum control and coherence protection of tin-vacancy spin qubits in a strain-tuned diamond-membrane heterostructure, *Phys. Rev. X* 13 (2023) 041037. doi:10.1103/PhysRevX.13.041037. URL <https://link.aps.org/doi/10.1103/PhysRevX.13.041037>
- [70] Y.-I. Sohn, S. Meesala, B. Pingault, H. A. Atikian, J. Holzgrafe, M. Gündoğan, C. Stavrakas, M. J. Stanley, A. Sipahigil, J. Choi, M. Zhang, J. L. Pacheco, J. Abraham, E. Bielejec, M. D. Lukin, M. Atatüre, M. Lončar, Controlling the coherence of a diamond spin qubit through its strain environment, *Nature Communications* 9 (1) (May 2018). doi:10.1038/s41467-018-04340-3. URL <http://dx.doi.org/10.1038/s41467-018-04340-3>
- [71] M. Klotz, K. G. Fehler, R. Waltrich, E. S. Steiger, S. Häußler, P. Reddy, L. F. Kulikova, V. A. Davydov, V. N. Agafonov, M. W. Doherty, A. Kubanek, Prolonged orbital relaxation by locally modified phonon density of states for the siv⁻ center in nanodiamonds, *Phys. Rev. Lett.* 128 (2022) 153602. doi:10.1103/PhysRevLett.128.153602. URL <https://link.aps.org/doi/10.1103/PhysRevLett.128.153602>
- [72] K. Kuruma, B. Pingault, C. Chia, M. Haas, G. D. Joe, D. R. Assumpcao, S. W. Ding, C. Jin, C. J. Xin, M. Yeh, N. Sinclair, M. Lončar, Controlling interactions between high-frequency phonons and single quantum systems using phononic crystals, *Nature Physics* 21 (1) (2024) 77–82. doi:10.1038/s41567-024-02697-5. URL <http://dx.doi.org/10.1038/s41567-024-02697-5>

- [73] M. Kasha, Characterization of electronic transitions in complex molecules, *Discussions of the Faraday Society* 9 (1950) 14. doi:10.1039/df9500900014. URL <http://dx.doi.org/10.1039/DF9500900014>
- [74] M. Kasha, S. P. McGlynn, Molecular electronic spectroscopy, *Annual Review of Physical Chemistry* 7 (1) (1956) 403–424. doi:10.1146/annurev.pc.07.100156.002155. URL <http://dx.doi.org/10.1146/annurev.pc.07.100156.002155>
- [75] A. Liu, S. T. Cundiff, D. B. Almeida, R. Ulbricht, Spectral broadening and ultrafast dynamics of a nitrogen-vacancy center ensemble in diamond, *Materials for Quantum Technology* 1 (2) (2021) 025002. doi:10.1088/2633-4356/abf330. URL <http://dx.doi.org/10.1088/2633-4356/abf330>
- [76] R. Ulbricht, S. Dong, A. Gali, S. Meng, Z.-H. Loh, Vibrational relaxation dynamics of the nitrogen-vacancy center in diamond, *Phys. Rev. B* 97 (2018) 220302. doi:10.1103/PhysRevB.97.220302. URL <https://link.aps.org/doi/10.1103/PhysRevB.97.220302>
- [77] V. M. Huxter, T. A. A. Oliver, D. Budker, G. R. Fleming, Vibrational and electronic dynamics of nitrogen-vacancy centres in diamond revealed by two-dimensional ultrafast spectroscopy, *Nature Physics* 9 (11) (2013) 744–749. doi:10.1038/nphys2753. URL <http://dx.doi.org/10.1038/nphys2753>
- [78] R. Ulbricht, S. Dong, I.-Y. Chang, B. M. K. Mariserla, K. M. Dani, K. Hyeon-Deuk, Z.-H. Loh, Jahn-teller-induced femtosecond electronic depolarization dynamics of the nitrogen-vacancy defect in diamond, *Nature Communications* 7 (1) (Nov. 2016). doi:10.1038/ncomms13510. URL <http://dx.doi.org/10.1038/ncomms13510>
- [79] W. P. Carbery, C. A. Farfan, R. Ulbricht, D. B. Turner, The phonon-modulated jahn-teller distortion of the nitrogen vacancy center in diamond, *Nature Communications* 15 (1) (Oct. 2024). doi:10.1038/s41467-024-52712-9. URL <http://dx.doi.org/10.1038/s41467-024-52712-9>
- [80] J. Eng, C. Gourlaouen, E. Gindensperger, C. Daniel, Spin-vibronic quantum dynamics for ultrafast excited-state processes, *Accounts of Chemical Research* 48 (3) (2015) 809–817. doi:10.1021/ar500369r. URL <http://dx.doi.org/10.1021/ar500369r>
- [81] A. E. Rugar, S. Aghaeimeibodi, D. Riedel, C. Dory, H. Lu, P. J. McQuade, Z.-X. Shen, N. A. Melosh, J. Vučković, Quantum photonic interface for tin-vacancy centers in diamond, *Phys. Rev. X* 11 (2021) 031021. doi:10.1103/PhysRevX.11.031021. URL <https://link.aps.org/doi/10.1103/PhysRevX.11.031021>
- [82] G. m. H. Thiering, A. Gali, Erratum: Ab initio magneto-optical spectrum of group-iv vacancy color centers in diamond [*phys. rev. x* 8, 021063 (2018)], *Phys. Rev. X* 10 (2020) 039901. doi:10.1103/PhysRevX.10.039901. URL <https://link.aps.org/doi/10.1103/PhysRevX.10.039901>
- [83] P. E. Blöchl, Projector augmented-wave method, *Phys. Rev. B* 50 (1994) 17953–17979. doi:10.1103/PhysRevB.50.17953. URL <https://link.aps.org/doi/10.1103/PhysRevB.50.17953>
- [84] G. Kresse, D. Joubert, From ultrasoft pseudopotentials to the projector augmented-wave method, *Phys. Rev. B* 59 (1999) 1758–1775. doi:10.1103/PhysRevB.59.1758. URL <https://link.aps.org/doi/10.1103/PhysRevB.59.1758>
- [85] D. Hobbs, G. Kresse, J. Hafner, Fully unconstrained noncollinear magnetism within the projector augmented-wave method, *Phys. Rev. B* 62 (2000) 11556–11570. doi:10.1103/PhysRevB.62.11556. URL <https://link.aps.org/doi/10.1103/PhysRevB.62.11556>
- [86] F. Neese, Efficient and accurate approximations to the molecular spin-orbit coupling operator and their use in molecular g-tensor calculations, *The Journal of Chemical Physics* 122 (3) (Jan. 2005). doi:10.1063/1.1829047. URL <http://dx.doi.org/10.1063/1.1829047>
- [87] F. Bruder, Y. J. Franzke, F. Weigend, Paramagnetic nmr shielding tensors based on scalar exact two-component and spin-orbit perturbation theory, *The Journal of Physical Chemistry A* 126 (30) (2022) 5050–5069. doi:10.1021/acs.jpca.2c03579. URL <http://dx.doi.org/10.1021/acs.jpca.2c03579>
- [88] Y. J. Franzke, J. M. Yu, Quasi-relativistic calculation of epr g tensors with derivatives of the decoupling transformation, gauge-including atomic orbitals, and magnetic balance, *Journal of Chemical Theory and Computation* 18 (4) (2022) 2246–2266. doi:10.1021/acs.jctc.1c01175. URL <http://dx.doi.org/10.1021/acs.jctc.1c01175>
- [89] O. Bengone, M. Alouani, P. Blöchl, J. Hugel, Implementation of the projector augmented-wave lda+u method: Application to the electronic structure of nio, *Phys. Rev. B* 62 (2000) 16392–16401. doi:10.1103/PhysRevB.62.16392. URL <https://link.aps.org/doi/10.1103/PhysRevB.62.16392>
- [90] O. Bulancea-Lindvall, J. Davidsson, I. G. Ivanov, A. Gali, V. Ivády, R. Armiento, I. A. Abrikosov, Temperature dependence of the ab lines and optical properties of the carbon-antisite-vacancy pair in 4h-SiC, *Phys. Rev. Appl.* 22 (2024) 034056. doi:10.1103/PhysRevApplied.22.034056. URL <https://link.aps.org/doi/10.1103/PhysRevApplied.22.034056>
- [91] Y. Xiong, G. Hautier, δ scf in VASP for excited-state defect computations: tips and pitfalls (2025). arXiv:2505.04748. URL <https://arxiv.org/abs/2505.04748>
- [92] J. P. Perdew, K. Burke, M. Ernzerhof, Generalized gradient approximation made simple, *Phys. Rev. Lett.* 77 (1996) 3865–3868. doi:10.1103/PhysRevLett.77.3865. URL <https://link.aps.org/doi/10.1103/PhysRevLett.77.3865>
- [93] J. Heyd, G. E. Scuseria, M. Ernzerhof, Hybrid functionals based on a screened coulomb potential, *The Journal of Chemical Physics* 118 (18) (2003)

- 8207–8215. arXiv:https://pubs.aip.org/aip/jcp/article-pdf/118/18/8207/19093575/8207_1_online.pdf, doi:10.1063/1.1564060. URL <https://doi.org/10.1063/1.1564060>
- [94] A. V. Krukau, O. A. Vydrov, A. F. Izmaylov, G. E. Scuseria, Influence of the exchange screening parameter on the performance of screened hybrid functionals, *The Journal of Chemical Physics* 125 (22) (2006) 224106. arXiv:https://pubs.aip.org/aip/jcp/article-pdf/doi/10.1063/1.2404663/13263224/224106_1_online.pdf, doi:10.1063/1.2404663. URL <https://doi.org/10.1063/1.2404663>
- [95] M. N. R. Ashfold, J. P. Goss, B. L. Green, P. W. May, M. E. Newton, C. V. Peaker, Nitrogen in diamond, *Chemical Reviews* 120 (12) (2020) 5745–5794. doi:10.1021/acs.chemrev.9b00518. URL <https://doi.org/10.1021/acs.chemrev.9b00518>
- [96] A. M. Zaitsev, *Optical Properties of Diamond*, Springer Berlin, Heidelberg, 2001.
- [97] M. Babamoradi, S. Asgari, A. Ranjbar, R. V. Belosludov, S. Yunoki, Many-electron states of the n2 and n3 color centers in diamond: A first- principles and many-body study, *Physica B: Condensed Matter* 505 (2017) 17–21. doi:<https://doi.org/10.1016/j.physb.2016.10.021>. URL <https://www.sciencedirect.com/science/article/pii/S0921452616304835>
- [98] J. P. Goss, R. Jones, S. J. Breuer, P. R. Briddon, S. Öberg, The twelve-line 1.682 eV luminescence center in diamond and the vacancy-silicon complex, *Phys. Rev. Lett.* 77 (1996) 3041–3044. doi:10.1103/PhysRevLett.77.3041. URL <https://link.aps.org/doi/10.1103/PhysRevLett.77.3041>
- [99] C. Adamo, V. Barone, Toward reliable density functional methods without adjustable parameters: The pbe0 model, *The Journal of Chemical Physics* 110 (13) (1999) 6158–6170. doi:10.1063/1.478522. URL <https://doi.org/10.1063/1.478522>
- [100] K. Sharma, O. A. Vasilyev, J. F. Stanton, T. A. Miller, Ab initio simulation of spin-vibronic spectra of methoxy radical, *The Journal of Chemical Physics* 162 (18) (2025) 184103. doi:10.1063/5.0266367. URL <https://doi.org/10.1063/5.0266367>
- [101] D. A. Matthews, J. F. Stanton, A new approach to approximate equation-of-motion coupled cluster with triple excitations, *The Journal of Chemical Physics* 145 (12) (2016) 124102. doi:10.1063/1.4962910. URL <https://doi.org/10.1063/1.4962910>
- [102] Y. Lee, G. Wann, Y. Lee, Vibronic analysis of the $\tilde{A} \rightarrow \tilde{X}$ laser-induced fluorescence of jet-cooled methoxy (ch3o) radical, *The Journal of Chemical Physics* 99 (12) (1993) 9465–9471. doi:10.1063/1.465481. URL <https://doi.org/10.1063/1.465481>
- [103] S. Bhattacharyya, D. Opalka, L. V. Poluyanov, W. Domcke, Jahn-teller theory beyond the standard model, *Journal of Physics: Conference Series* 428 (2013) 012015. doi:10.1088/1742-6596/428/1/012015. URL <http://dx.doi.org/10.1088/1742-6596/428/1/012015>
- [104] G. Thiering, A. Gali, Spin-orbit coupling and jahn-teller effect in t_d symmetry: an ab initio study on the substitutional nickel defect in diamond, *Philosophical Transactions of the Royal Society A: Mathematical, Physical and Engineering Sciences* 382 (2265) (Dec. 2023). doi:10.1098/rsta.2022.0310. URL <http://dx.doi.org/10.1098/rsta.2022.0310>
- [105] G. Herrero-Saboya, L. Martin-Samos, N. Richard, A. Hemeryck, Common defects in diamond lattices as instances of the general $t \otimes (e + t_2)$ jahn-teller effect, *Phys. Rev. Mater.* 6 (2022) 034601. doi:10.1103/PhysRevMaterials.6.034601. URL <https://link.aps.org/doi/10.1103/PhysRevMaterials.6.034601>
- [106] J. C. A. Prentice, B. Monserrat, R. J. Needs, First-principles study of the dynamic jahn-teller distortion of the neutral vacancy in diamond, *Phys. Rev. B* 95 (2017) 014108. doi:10.1103/PhysRevB.95.014108. URL <https://link.aps.org/doi/10.1103/PhysRevB.95.014108>
- [107] I. B. Bersuker, Pseudo-jahn-teller effect—a two-state paradigm in formation, deformation, and transformation of molecular systems and solids, *Chemical Reviews* 113 (3) (2013) 1351–1390. doi:10.1021/cr300279n. URL <http://dx.doi.org/10.1021/cr300279n>
- [108] J. Coutinho, V. J. B. Torres, K. Demmouche, S. Öberg, Theory of the carbon vacancy in 4h-sic: Crystal field and pseudo-jahn-teller effects, *Phys. Rev. B* 96 (2017) 174105. doi:10.1103/PhysRevB.96.174105. URL <https://link.aps.org/doi/10.1103/PhysRevB.96.174105>
- [109] G. m. H. Thiering, A. Gali, Theory of the optical spin-polarization loop of the nitrogen-vacancy center in diamond, *Phys. Rev. B* 98 (2018) 085207. doi:10.1103/PhysRevB.98.085207. URL <https://link.aps.org/doi/10.1103/PhysRevB.98.085207>
- [110] I. B. Bersuker, Jahn-teller and pseudo-jahn-teller effects: From particular features to general tools in exploring molecular and solid state properties, *Chemical Reviews* 121 (3) (2020) 1463–1512. doi:10.1021/acs.chemrev.0c00718. URL <http://dx.doi.org/10.1021/acs.chemrev.0c00718>
- [111] Q. C. Qiu, L. F. Chibotaru, A. Ceulemans, Product jahn-teller systems: The $T_1 \otimes H \otimes (g + 2h)$ icosahedral exciton, *Phys. Rev. B* 65 (2001) 035104. doi:10.1103/PhysRevB.65.035104. URL <https://link.aps.org/doi/10.1103/PhysRevB.65.035104>
- [112] G. Thiering, A. Gali, The $(e_g \oplus e_u) \otimes eg$ product jahn-teller effect in the neutral group-iv vacancy quantum bits in diamond, *npj Computational Materials* 5 (1) (Feb. 2019). doi:10.1038/s41524-019-0158-3. URL <http://dx.doi.org/10.1038/s41524-019-0158-3>

- [113] C. J. Ciccarino, J. Flick, I. B. Harris, M. E. Trusheim, D. R. Englund, P. Narang, Strong spin–orbit quenching via the product jahn–teller effect in neutral group iv qubits in diamond, *npj Quantum Materials* 5 (1) (Oct. 2020). doi:10.1038/s41535-020-00281-7.

URL <http://dx.doi.org/10.1038/s41535-020-00281-7>